Interpretation of Refraction Images in Synchrotron Based Imaging Techniques Using Growth Plate Injury Specimens in an Animal Model

A Thesis Submitted to the College of Graduate Studies and Research in Partial Fulfillment of the Requirements for the Degree of Master of Science in the

Department of Anatomy and Cell Biology

College of Medicine, University of Saskatchewan

Saskatoon

By

Sheldon Wiebe

PERMISSION TO USE

In presenting this thesis in partial fulfillment of the requirements of a Master of Science degree from the University of Saskatchewan, I agree that the Libraries of this university may make it freely available for inspection. I further agree that permission for copying of this thesis in any manner, in whole or in part, for scholarly purposed may be granted by the professors who supervised my thesis work or, in their absence, by the Head of the Department of Anatomy and Cell Biology or the Dean of the College of Medicine. It is understood that any copying or publication or use of this thesis or parts thereof for financial gain shall not be allowed without written permission. It is understood that due recognition shall be given to me and the University of Saskatchewan in any scholarly use which may be made of any materials in my thesis.

Requests for permission to copy or make other use of material in this thesis in whole or in part should be addressed to:

Head, Department of Anatomy and Cell Biology

College of Medicine

University of Saskatchewan

107 Wiggins Road

Saskatoon, SK. S7N 5E5

CANADA

Abstract

Typical clinical radiography uses the variable absorption of x-radiation of different tissues within the object to produce contrast in the image. The interpretation of this image is based on understanding the anatomy and pathology as well as understanding how the image is produced. One needs to understand what features of the image are representative of the anatomy/pathology, what is inherent to the imaging process and what is artefact. The correlation of contrast in the image with absorption contrast in the object is fairly intuitive.

Diffraction Enhanced Imaging (DEI) uses the bending or refraction of radiation as it passes through a tissue interface to produce the contrast in the image in addition to absorption. The ability to interpret the refraction contrast image is not as intuitive as the absorption image. Edges are enhanced and tissues with different densities can look similar. Understanding the image acquisition of refraction based radiography also is not as intuitive as typical absorption radiography.

One potential advantage of DEI is the ability to visualize small structures that may not be visible using absorption radiography. The growth plate of long bones and the premature closure or bone bridge/bar formation across the growth plate associated with a fracture was targeted as a study sample.

An animal model (juvenile rat) was used for inducing a fracture through the proximal metaphysis of the tibia. The animal was then sacrificed at variable times of healing which is described below. The specimens were then imaged using DEI techniques at Brookhaven National Lab, Upton, New York, at the Biomedical Imaging and Therapy (BMIT) beamline at the Canadian Light Source and using a laboratory based DEI system at Nesch, LLC, Crown Point, Indiana.

High resolution absorption images were obtained using a SkyScan micro-CT from Prof. Cooper's laboratory for comparison of DEI and absorption images. Histological slides were also prepared for correlation of image anatomy.

The reason for imaging these specimens using different techniques was to determine potential translation of synchrotron based techniques with lab based or conventional techniques as well as determining what features of imaging could be uniquely done at a synchrotron. Since access to synchrotron biomedical imaging facilities is limited, the potential for some work to be done outside of synchrotron facilities would make research progress more efficient.

A detailed analysis of the images was performed. The detail of the bone as well as the fracture was exquisite with the CT data. With the planar images the orientation of the trabeculae of the bone relative to the direction of the analyser crystal (direction of diffraction) changes the appearance and texture of the bone image. It was hoped to visualize the layers of the growth plate (variable calcification) and perhaps the initiation of bone spicules leading to bone bridges across the growth plates at the site of fracture. However, the small size of the object limited observable detail.

This work was originally intended to apply a unique imaging technique for the study of growth plate fracture pathophysiology. However, it became clear that the technical image production and interpretation was more important to the project than the individual analysis of each specimen. As a result not all specimens were used, but those selected were used to refine the technique and interpret the synchrotron based images compared to conventional images.

The use of DEI for assessing bone bridge formation was promising, but the specimen size limited detail and resolution. This has led to the conclusion that a larger animal model would be more appropriate for this type of study.

Further, it was discovered that the bone (growth plate) orientation affected the planar image contrast of the bone / cartilage interface based on long axis orientation relative to the refraction sensitive direction of the DEI system. To more fully exploit this effect, more images at different object orientations would be necessary for interpretation in future work with larger animal models.

Acknowledgements

Co-Supervisors: Dr. Dean Chapman, Professor, Dept. Anatomy and Cell Biology and Dr. Bernhard Juurlink, Professor, College of Medicine, University of Alfaisal University, Riyadh, Kingdom of Saudi Arabia

Advisory Committee: Dr. William Kulyk (Chair), Professor, Dept. of Anatomy and Cell Biology; Dr. Alan Rosenberg, Professor, Dept. of Pediatrics; Dr. Graham George, Professor, Dept. Geological Sciences

Biomedical Imaging and Therapy Beamline, Canadian Light Source

Experimental data collected at this facility with experimental support from Dr. E. Schültke and Dr. D. Cooper and Dr. B. Bewer

National Synchrotron Light Source, Brookhaven National Labs

Experimental data collected at this facility with experimental support from Dr. Z. Zhong and E. Zhang, MD

Dedication

To Maryam, Zane, Dean and Aydin.

Table of Contents

List of Figures

List of Abbreviations

BMIT - Biomedical Imaging and Therapy Beamline at the Canadian Light Source

CLS - Canadian Light Source

CT - Computed Tomography

DEI - Diffraction Enhanced Imaging

microCT – micron scale resolution absorption Computed Tomography

PET-CT – Positron Emission Tomography-Computed Tomography

MRI – Magnetic Resonance Imaging

µRad – Micro-Radian: The ratio between the length of an arc and its radius. The radian is the standard unit of angular measurement. One radian equals 180/π degrees or approximately 57.2968°

List of Symbols

α	Real part of the refractive index (dimensionless)
β	Imaginary part of the refractive index (dimensionless)
C_{abs}	Absorption contrast (dimensionless or in percent)
d_{hkl}	Lattice plane spacing for (h,k,l) lattice planes (nm (10^{-9} m) are typical units)
e	Base of natural logarithms = 2.71828
$\left\|F_{hkl}\right\|$	Magnitude of the structure for the (h,k,l) reflection (dimensionless)
(h,k,l)	Indices (Miller indices) identifying lattice planes in a crystal (dimensionless triplet of integer numbers)

θ_B	Bragg angle for x-rays incident on a set of lattice planes (degrees or radians are typical units)
θ_A	Analyzer crystal angle for x-rays incident on a set of lattice planes (degrees or radians are typical units)
θ_L	Analyzer crystal angle for the low angle setting on the rocking curve (degrees or radians are typical units)
θ_H	Analyzer crystal angle for the high angle setting on the rocking curve (degrees or radians are typical units)
$\Delta\theta_{REF}$	Refraction deflection angle (angle measured relative to incident beam) (units are typically microradian = 10^{-6} radian = 57.3×10^{-6} degree)
λ	X-ray wavelength (nm (10^{-9} m) are typical units)
$\frac{\mu}{\rho}$	Mass attenuation coefficient for a material (cm^2/g are typical units)
$\frac{\mu}{\rho}_{Total}$	Total mass attenuation coefficient for a material (cm^2/g are typical units)
$\frac{\mu}{\rho}_{Coherent}$	Contribution to the mass attenuation coefficient from coherent scattering for a material (cm^2/g are typical units)
$\frac{\mu}{\rho}_{Compton}$	Contribution to the mass attenuation coefficient from Compton scattering for a material (cm^2/g are typical units)
$\frac{\mu}{\rho}_{Photoelectric}$	Contribution to the mass attenuation coefficient from photoelectric absorption for a material (cm^2/g are typical units)

$\frac{\mu}{\rho}_b$	Total mass attenuation coefficient for the background material (cm^2/g are typical units)
$\frac{\mu}{\rho}_f$	Total mass attenuation coefficient for the feature material (cm^2/g are typical units)
n	Refractive index for a material (dimensionless and complex)
N	Photon count (photon number - dimensionless)
N_b	Detected photon count in background region (photon number - dimensionless)
N_f	Detected photon count in feature region (photon number - dimensionless)
N_{AABS}	Photon count in a pixel for the DEI apparent absorption image (dimensionless photon count)
$\frac{\Delta N}{N}_{REF}$	Refraction contrast (dimensionless or percent)
$\frac{dR}{d\theta}$	Slope of crystal rocking curve (units are typically inverse microradians (μr^{-1}))
$\frac{dR}{d\theta}\left(\theta_{L,H}\right)$	Slope of crystal rocking curve on the low (L subscript) or high (H subscript) side of the analyzer rocking curve (units are typically inverse microradians (μr^{-1}))
ρ	Mass density for a material (g/cm^3 are typical units)
ρ_b	Mass density for the background material (g/cm^3 are typical units)
ρ_f	Mass density for the feature material (g/cm^3 are typical units)
t	Thickness of a material (cm are typical units)
t_b	Thickness of the background material (cm are typical units)
r_e	Classical electron radius = 2.81×10^{-15} m = 2.81×10^{-6} nm

$\frac{\partial t}{\partial z}$	Gradient of a material thickness along the z direction (dimensionless units)
u	Nucleon mass (1.67×10^{-27} kg $= 1.67 \times 10^{-24}$ g)
V_C	Unit cell volume for a crystal lattice ($nm^3 = 10^{-27}$ m^3 are typical units)
ω_D	Darwin width of a crystal reflection (units are typically microradians (μr))
Z	Elemental proton count (dimensionless)

HYPOTHESIS

Synchrotron imaging methods can provide detailed images of the micro-anatomy of the growth plate of long bones and will detect the small bone structures indicative of healing earlier than is possible with current imaging modalities.

Additionally, osseous microstructures including layers of the growth plate and early detection of bone bridge formation across the injured growth plate are detectable using DEI techniques which will have better contrast and image resolution than with x-ray absorption imaging.

1 Introduction

1.1 Overview

This thesis is directed to the use of synchrotron imaging methods for the study of growth plate fracture research. Growth plate fractures can produce growth deformities in some children who experience an injury or fracture through the growth plate before it closes. In approximately a quarter of patients who experience a fracture through the growth plate, a bone bridge or bar forms across the growth plate which then tethers the epiphysis and prevents elongation of the long bone during growth. The younger the child the more potential there is for a deformity, such as leg length discrepancy due to a longer period of growth subsequent to the injury.

The original goal of this research was to investigate if synchrotron imaging methods could be used to follow the progression of fracture repair and the bony growths that occur during the repair. Additionally, due to worldwide limited availability of synchrotron biomedical facilities where such studies could be carried out, as well as for correlation with imaging findings with non-synchrotron DEI imaging based systems, it was felt that evaluating alternative conventional x-ray source DEI imaging systems would be an important aspect to investigate. More accessible DEI imaging technology would facilitate research in this area. Accordingly, I undertook to evaluate two alternatives in parallel with my synchrotron studies; a synchrotron spin-off of DEI (Nesch, LLC) based imaging system and a laboratory-based micro computed tomography system (SkyScan desk top scanner). Results from the synchrotron study, the laboratory based micro computed tomography and the Nesch DEI systems are part of this thesis.

Comparing data from conventional imaging techniques and the synchrotron based techniques is also important. Similar to a century ago when x-rays were first used to diagnose medical conditions and in the last number of decades each time a new modality is developed, extensive work is done to compare the new images with conventional imaging (for the time) as well as with histology or pathology. This becomes essential in the interpretation of the images for the purposes of diagnosis, monitoring and treatment. It is recognized that this thesis is not comprehensive with respect to all imaging modalities,

but does represent how to begin interpreting DEI and the start of a system of correlation of synchrotron produced images with established techniques.

Similar to conventional absorption x-ray imaging the thicker the tissue imaged in a plane, the more artefact results from "noise". However, in DEI it is refraction events that take place which produce noise or artefact, instead of Compton scatter that may not represent a true image of the tissue. One way to reduce the effect is to use DEI CT which is able to provide slices through a subject similar to absorption x-ray CT and provide detailed refraction contrast. As mentioned, there are challenges related to a fixed x-ray source (the need to spin the object in order to produce the CT dataset). Without the ability to move the x-ray source there is the need to spin the subject which can produce technical challenges. Additionally the amount of time required to obtain DEI-CT data can be associated with concerning radiation dose exposures in living animals.

1.2 Thesis Organization

This thesis is organized in the following way.

Chapter 2 gives background for understanding the DEI process as well how it develops contrast in biological or soft tissue systems. Chapter 2 also includes background on the importance and implications of growth plate fracture and clinical relevance.

Chapter 3 gives a detailed description of the experiments performed. This includes information on the fracture model used and a description of the imaging methods performed. Those include DEI (both synchrotron and laboratory based) in both planar and CT modes as well as laboratory based microCT.

The interpretation of the refraction images has not been presented previously in any known work. For accurate interpretation of refraction images a framework for understanding these images is described.

The experimental results from the various imaging modalities are reported in Chapter 4. Those include synchrotron DEI imaging from Brookhaven National Laboratory in both projection and CT modes, projection imaging results using a laboratory based DEI system at Nesch, LLC, initial DEI projection imaging at the newly commissioned BMIT facility at the Canadian Light Source and high resolution microCT in Prof. David Cooper's laboratory.

The relevance and importance of the work are discussed in Chapter 5.

Concluding remarks are given in Chapter 6 and remaining issues to be resolved are included a future work chapter (Chapter 7).

References are given in Chapter 8.

2 Background

2.1 X-ray Imaging

Conventional x-ray radiography has it origin with the discovery of x-rays by Roentgen in 1896 (Roentgen, 1896). The high penetrating power of this type of radiation allowed internal structures within objects to be visualized. The imaging system that allowed this method to be used was somewhat simple with an x-ray source, object to be imaged and a detector such as a film plate used to record the information. This basic arrangement is still used today with many advances in x-ray tube technology, anti-scatter techniques to improve image contrast and detector technology which is now almost exclusively digital in nature (Oppelt, 2005). As with any imaging modality, there must be some physical mechanism that allows the object to be imaged. In the case of conventional clinical radiography, the mechanism that allows features to be imaged is based on x-ray attenuation. It is absorption differences between various tissues that allow them to be visualized. These absorption differences result in differing transmitted intensities across the imaging field which when recorded in a detector (film or digital) result in contrast in the image. Image contrast is defined as the change in recorded image values across a structural feature within the imaging field compared to what is considered to be a background value (Bushberg *et al.*, 2001). If the detector records transmitted intensity values (i.e. number of photons recorded in each detector element or pixel) then the contrast would be a comparison of the photon count in one detector element at the location corresponding to a structure compared to that of a detector pixel element in a region away from that location. Specifically, a detector element corresponding to the feature object records a value, N_f, and nearby in a background region the detector records a value N_b, the contrast, C, is

$$C = \frac{N_f - N_b}{N_b} \quad .$$ **Equation 1**

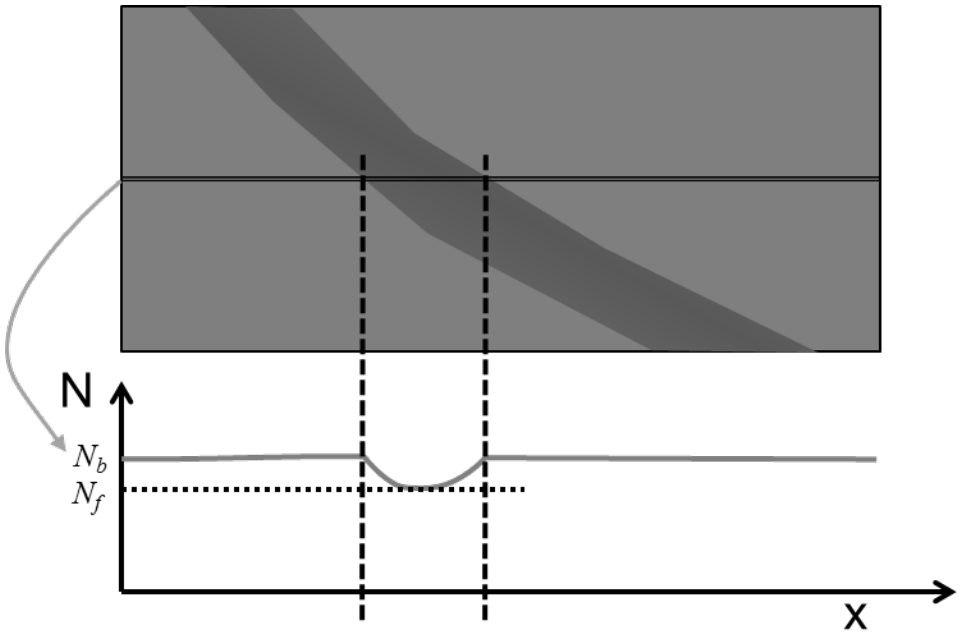

Figure 1 An example of physical meaning of image contrast for an intensity based image. The horizontal line cuts across an image feature in the upper part of the figure; the lower part shows a line plot of the measured photon count. N_b represents the background photon count value and N_f the photon count within the feature.

The contrast is then a value that has a range from 0, no contrast or no feature visibility to 1, total visibility. Figure 1 shows a schematic representation of an image and the image contrast arising from an embedded feature structure.

As mentioned, conventional x-ray radiography relies on the attenuation of x-rays to develop image contrast. There are several mechanisms that can lead to attenuation of x-rays in matter or tissue (Hendee and Ritenour, 2002). In the x-ray energy range used in diagnostic radiography there are primarily three physical mechanisms of x-ray attenuation; photoelectric absorption, Compton scattering and coherent scattering.

A metric of the attenuation is the mass attenuation coefficient, $\frac{\mu}{\rho}$, a quantity which is independent of the state of the material. For example, the $\frac{\mu}{\rho}$ of water is the same if water is in the form of ice, liquid or steam. In the diagnostic imaging photon energy range, the $\frac{\mu}{\rho}$ is comprised of three parts listed earlier which sum to form the total mass attenuation coefficient, $\frac{\mu}{\rho}_{Total}$. Specifically,

$$\frac{\mu}{\rho}_{Total} = \frac{\mu}{\rho}_{Photoelectric} + \frac{\mu}{\rho}_{Compton} + \frac{\mu}{\rho}_{Coherent}, \quad \textbf{Equation 2}$$

where the subscripts to each term identify the mechanism of attenuation which will be discussed below.

Photoelectric absorption is a physical mechanism of interaction between a light quantum or photon and a bound electron in an atom of matter. In this interaction the photon is absorbed while ejecting the electron from the atom. For this interaction to occur, the photon quantum energy must exceed the binding energy of the electron. The binding energy is the minimum amount of energy required to extract an electron from the atom taking it from the bound state to a free or continuum state. In this process the photon is completely destroyed. This mechanism results in a contribution to x-ray attenuation that is strongly dependent on the number of electrons associated with atoms as well as the photon energy. The photoelectric attenuation is proportional to the atomic number (Z) cubed and inversely proportional to the photon energy cubed (Hendee and Ritenour, 2002). The photoelectric attenuation is large for high Z elements (i.e. Pb (lead), Z=82, is a good attenuation material) and at low x-ray energies. It is this property of high absorption at low energies that leads to the need to have relatively high x-ray energies for diagnostic imaging. This high absorption has practical consequences. First, at low x-ray energies there is little x-ray transmission, thus forming an image is difficult due to lack of x-rays passing through the object to the detector. Second, is the fact that high absorption of x-ray photons also then occurs in the object (tissues) that are being imaged which translates into high x-ray exposure or dose to the tissues or patient (absorbed dose).

The Compton Effect (Compton, 1923) also contributes to overall attenuation of photons. In this interaction, an x-ray photon strikes a weakly bound electron and there is an exchange of energy. This results in a lower energy photon being scattered past the electron as well as the electron being ejected or scattered. This effect results in scattered photons all with a lower energy and often a different direction than those photons incident on the material. The Compton attenuation coefficient is roughly energy independent in the photon energy range used in diagnostic imaging and is roughly independent of material (Hendee and Ritenour, 2002).

The scattered photons arising from Compton scattering is the major contributor to background noise in conventional x-ray imaging. Most conventional radiographic methods employ anti-scatter grids placed in front of the detector to absorb the lower energy photons that have changed direction from the

interaction with the tissue / object to reduce this scatter prior to detection. This reduction of

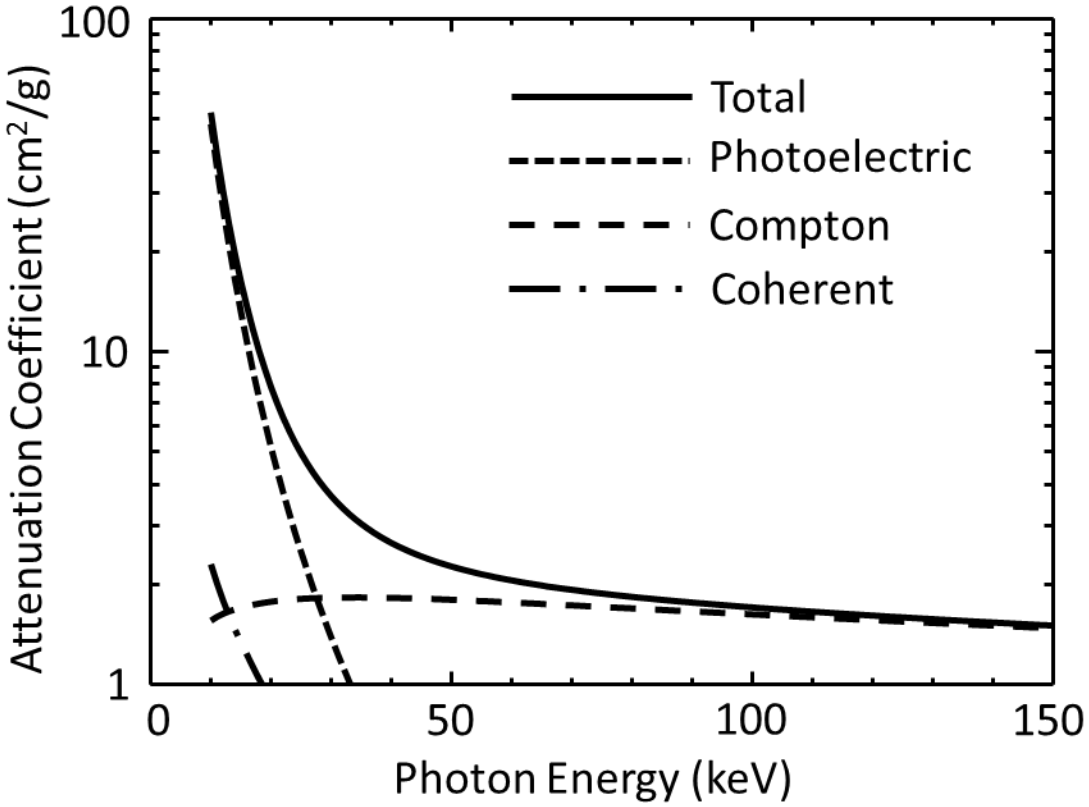

Figure 2 Attenuation coefficient for water over the diagnostic imaging energy range. Each of the contributions to the total attenuation coefficient (solid line) are indicated; Photoelectric (short dash line), Compton (long dash line), and Coherent (long and short dash line) (Chapman, 2011).

background radiation that interacts with the detector improves image contrast.

Finally, the attenuation contribution from coherent scattering is proportional to the elemental Z and the inverse energy squared.

The detailed contributions of each of these mechanisms depend on the specific material. However, for a material such as soft tissue, the photoelectric effect and Compton scattering are the dominant mechanisms with coherent scattering playing an insignificant role in attenuation. For soft tissue, the photoelectric effect will dominate at x-ray energies below approximately 30keV and Compton scattering dominating at higher x-ray energies. As an example the total attenuation coefficient for water is shown in Figure 2. Also shown in this figure are the contributions leading to the total attenuation arising from the photoelectric, Compton and coherent mechanisms. Note the transition from photoelectric behavior

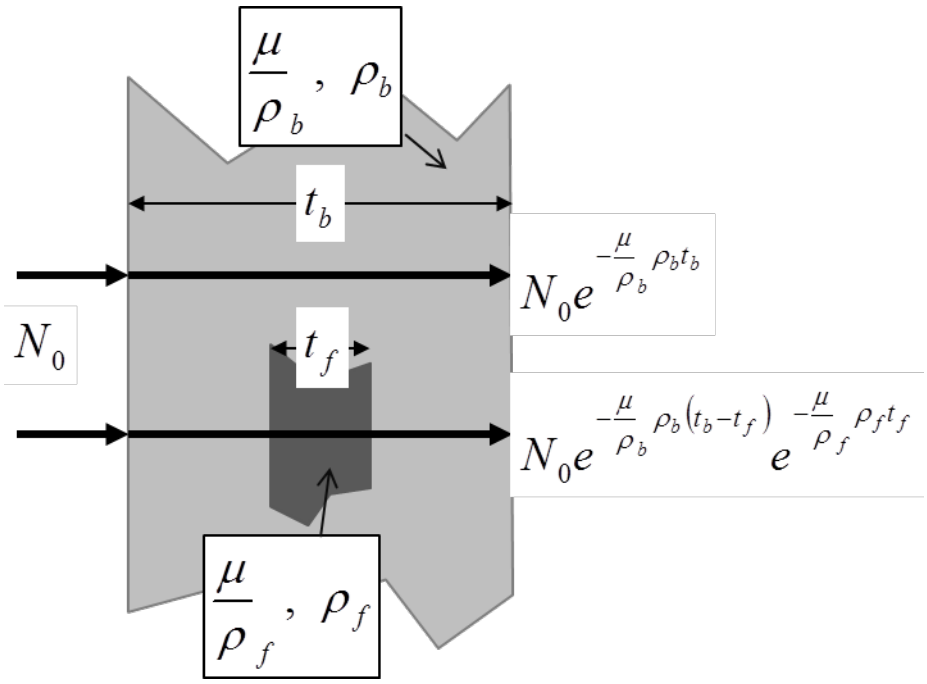

Figure 3 Attenuation contrast figure for an embedded object for an object composed of a background material (b subscript) and an embedded feature (f subscript).(Chapman, 2011)

below 30keV and the transition to Compton dominated above. Also note, the small role that coherent scattering plays in the total attenuation.

An understanding of these mechanisms is important because they define the contrast that arises from absorption based imaging as well as the origin of scatter which degrades contrast in conventional imaging. Also, these mechanisms play a role in our understanding of new imaging methods that derive both absorption contrast as well as contrast arising from phase or refraction effects. The interpretation of images requires a fundamental understanding of these principles in order to appreciate the relationship of the object to the image.

Contrast from attenuation can be calculated. For example, in Figure 3 we have an object with a mass structure (feature object, such as an organ within the body) within a larger object. The object has two materials, the background material and the feature embedded material. These two materials may have different attenuation coefficients and densities. The object will have some overall thickness and the embedded feature will have some thickness as well along the direction of the x-ray beam. The contrast arising from comparing the background detected photon count to that where the embedded mass is approximately,

$$C_{abs} \cong \left(\frac{\mu}{\rho}_f \rho_f - \frac{\mu}{\rho}_b \rho_b \right) t_f = \left(\mu_f - \mu_b \right) t_f \quad \text{Equation 3}$$

,

where the background material has a total attenuation of $\frac{\mu}{\rho}_b$, a density of ρ_b, the embedded feature has a total attenuation of $\frac{\mu}{\rho}_f$, a density of ρ_f, and a thickness of t_f.

Absorption contrast requires that the two materials have different linear attenuation coefficients. The linear attenuation coefficient difference can arise from a composition difference, a difference in densities or both. For example, bone has good absorption contrast compared to soft tissue due to both a composition difference and a density difference. Most cancerous tissues have a similar contrast compared to surrounding soft tissue because of a subtle density difference and little, if any, compositional difference.

2.2 Diffraction Enhanced X-ray Imaging

DEI (Chapman *et al.*, 1997) is an x-ray radiographic technique that provides dramatic gains in contrast over conventional radiography by utilizing x-ray refraction and scatter rejection as contrast mechanisms, in addition to the x-ray absorption utilized by conventional radiography. Images using DEI techniques have been acquired with unprecedented quality and clarity. Images of test objects, also known as phantoms (Gotzsche and Olsen, 2000), cancerous breast tissues (Pisano *et al.*, 2000; Hasnah *et al.*, 2002), lungs of rats (Zhong *et al.*, 2000b), and human excised cartilage as well as rabbit cartilage (Muehleman *et al.*, 2006) have been successfully imaged using DEI. DEI has augmented the image information content by allowing new physical parameters, namely x-ray refraction and extinction, to be imaged.

The interaction of x-rays with the subject includes not only the attenuation, but also refraction (Podurets *et al.*, 1989; Somenkov *et al.*, 1991; Ingal and Beliaevskaya, 1995) and small-angle scattering

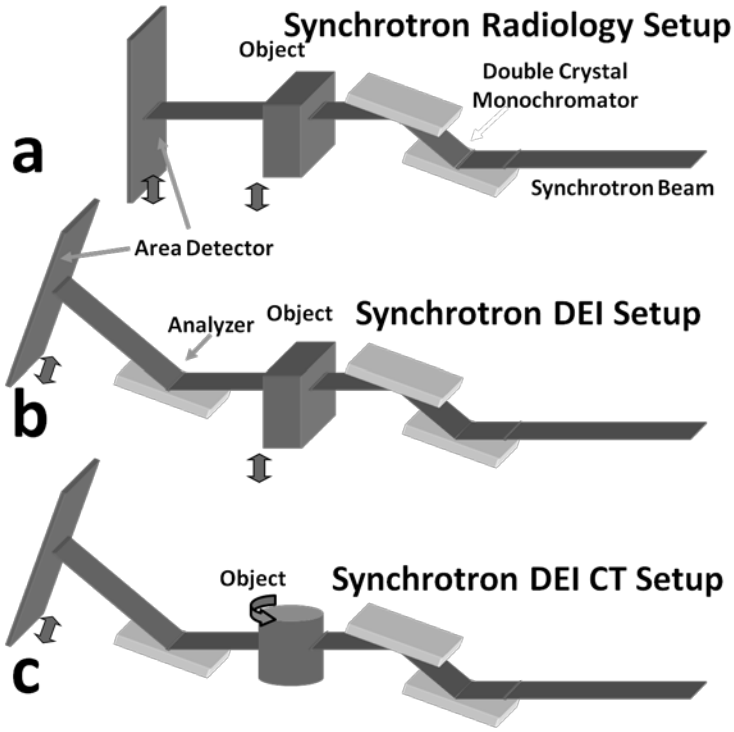

Figure 4 Schematic Experimental Setup: a) The synchrotron setup used to obtain radiographs of the object. b) DEI setup showing the addition of the analyzer crystal. c) DEI in the CT mode. In both figures, the polychromatic synchrotron beam enters from the right, passes through a double crystal monochromator where a narrow energy band is selected. The x-ray beam then passes through the object and onto a detector (a) or onto an analyzer crystal (b,c).

(Bushuev *et al.*, 1996). Both mechanisms carry information about the subject's structure on the length scale up to several microns. The information about the refraction and small angle scattering is lost in conventional radiography due to their small angle nature. Therefore, conventional radiography measures only the x-ray attenuation of the subject.

In DEI, an imaging beam is prepared by diffracting the polychromatic beam to create a nearly monochromatic beam (Chapman *et al.*, 1997; Zhong *et al.*, 2000b) using parallel crystals within a monochromator. This beam is then passed through the subject as in conventional radiography. However, a matching crystal is placed between the subject and the detector. This crystal (analyzer) is

set at or near the peak of the Bragg diffraction. A schematic representation of a synchrotron radiography and DEI system is shown in Figure 4a and Figure 4b, respectively. A CT arrangement is shown in Figure 4c.

X-ray diffraction from perfect crystals with a narrow reflection angular width on the order of a few microradians and peak reflectivity of close to unity, provides the tools necessary to prepare and analyze x-ray beams traversing an object on the microradian scale (Zhong *et al.*, 2000b). The condition for x-ray diffraction from the analyzer crystal is met only when the incident beam makes the correct angle to the atomic lattice planes in the crystal for a given x-ray energy or wavelength. When this condition is met the beam diffracts from the analyzer over a narrow range of incident angles. As the analyzer is rotated, the intensity variation observed is referred to as the rocking curve. The shape of this curve is roughly triangular.

Since the range of angles which can be accepted by the analyzer is only a few microradians, the analyzer provides scatter-rejection at the microradian level which is below the capabilities of conventional anti-scatter techniques such as slit collimation and grids. Small angle scattering arises from diffraction from structures with dimensions up to micron sizes. This scattering intensity, which would normally appear in the image, is missing and appears in the same way as absorption in the image. This scatter rejection contrast is called extinction contrast. Therefore, in DEI, the image which represents the absorption of the object by x-rays is referred to as the apparent absorption image since it has contrast derived from both absorption and scatter rejection, or extinction.

The analyzer rocking curve introduces sensitivity to refraction occurring within the object when the analyzer is de-tuned from the peak position on the shoulder of its rocking curve. Density, thickness and/or material variations in an object refract the x-rays as they cross through the material interface. These small angular variations are generally in the sub-microradian range. The steep sides of the rocking curve convert these subtle angle variations into intensity variations, thus making refraction effects visible in an image. By acquiring an image pair with the analyzer set to diffract on each side of the rocking curve, refraction effects have been separated from combined absorption and extinction (Chapman *et al.*, 1997). This process will be described in more detail in the following sections.

2.2.1 X-Ray Refraction

In the previous sections the interactions of x-rays with matter were discussed in the context of attenuation which allows a basic understanding of conventional x-radiography. In this section, another interaction will be described which affect the wave properties of x-rays as they propagate through matter. This interaction is important because it accounts for image contrast arising from an emerging area of x-ray imaging based on phase or refraction properties.

X-rays travel through material in nearly straight lines which contributes to its success in representing the internal structures of objects with different densities which Roentgen recognized in 1896. However, x-rays do have a refractive index which is close to and slightly less than 1 (with 1 being the index value in a vacuum). For the purposes of this discussion the refractive index, *n*, can be represented as having a small difference from 1. By convention the parameter α is that difference (Als-Nielsen and McMorrow, 2001).

$$n = 1 - \alpha - i\beta \qquad \textbf{Equation 4}$$

In Equation 4, the $1-\alpha$ term is the part responsible for x-ray refraction. The additional term ($i\beta$) is responsible for attenuation and is related to the mass attenuation coefficient, $\frac{\mu}{\rho}_{Tot}$.

For reference, values of these quantities are given in Table 1 for selected materials at 20 and 40keV.

	20keV			40keV		
Material	$\frac{\mu}{\rho}_{Tot}$ (cm^2/g)	α X10^{-6}	β X10^{-9}	$\frac{\mu}{\rho}_{Tot}$ (cm^2/g)	α X10^{-6}	β X10^{-9}
Water	0.783	0.576	0.386	0.267	0.144	0.0658
Bone	2.78	1.02	2.53	0.514	0.254	0.235
Air	0.855	0.000669	0.000545	0.259	0.000167	0.0000827
Al	3.42	1.36	4.56	0.566	0.338	0.377

Table 1 Values of total mass attenuation coefficient, α and β for water, bone, air and aluminum at 20 and 40 keV. Note the values in the α column are to be multiplied by 10^{-6}; values in the β column are to be multiplied by 10^{-9}.

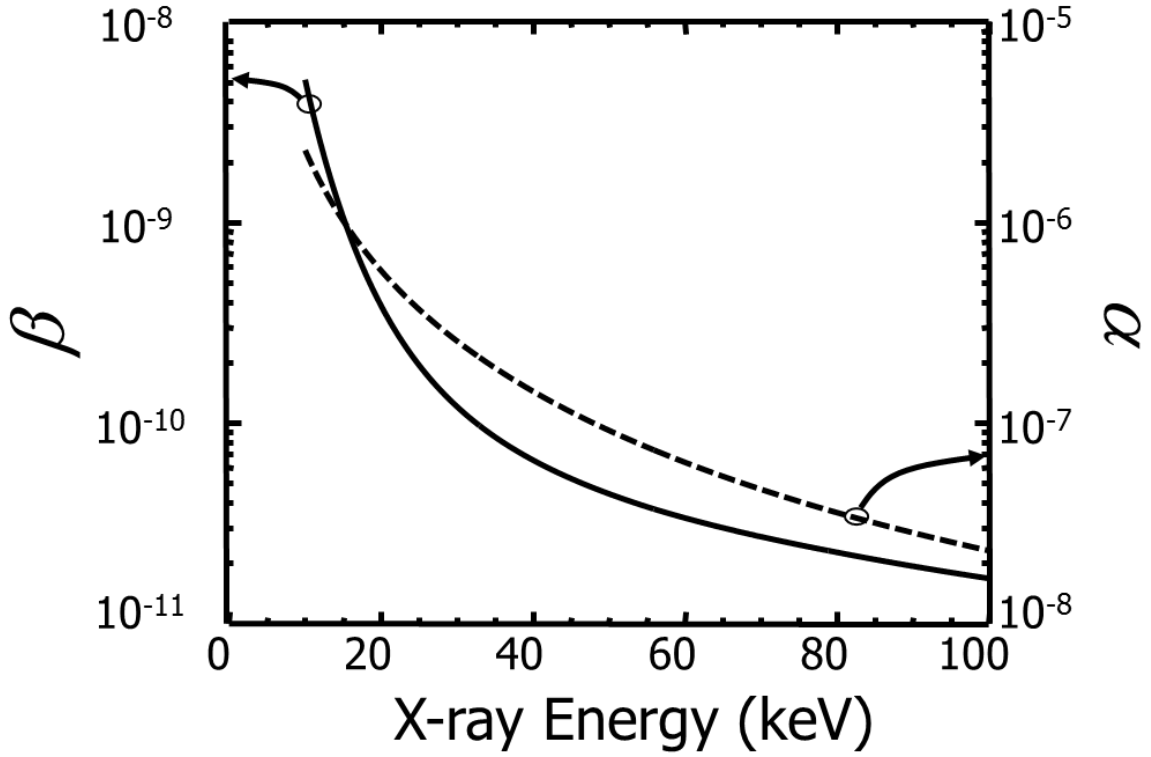

Figure 5 Comparison plot for both *α* and *β* over the energy range from 10 to 100keV. The *β* scale is on the left with the plot shown as the solid line. The *α* scale is on the right with the plot shown as the dashed line. Note that typically *α* is about three orders of magnitude larger than *β*. (Chapman, 2011)

As shown in Figure 5 the value of the real part of the refractive correction is about 1000 times larger than the imaginary part. This indicates that the potential for the use of refraction as a possible imaging contrast mechanism is better than absorption especially for small objects without a significant change in electron density with the adjacent material.

2.2.2 X-Ray Diffraction

As indicated in the introduction, the DEI system relies on x-ray diffraction from crystals. The concepts underlying x-ray diffraction will now be discussed briefly.

X-ray diffraction is based on constructive interference of x-ray photons as they interact with atoms or molecules in a regular arrangement such as a crystal. This phenomenon is understood by considering light scattering from what appear to be planes of atoms in a crystal. In a crystal all atoms are arranged periodically and that can be represented as planes of atoms. It is the realization that x-rays could be diffracted from these planes that led to the Bragg description of x-ray diffraction (Bragg, 1913b, a).

Assume that there are planes of atoms where each plane is separated from one another by a distance, d. Also assume that a fixed wavelength beam of light strikes these planes at an angle of incidence to the

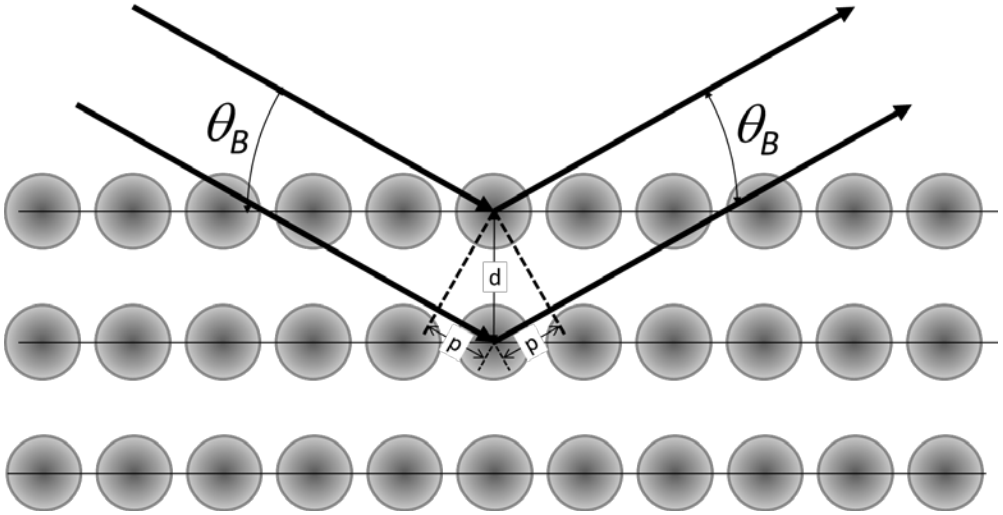

Figure 6 Schematic used to derive Bragg's Law for diffraction from lattice planes in a crystal. The incident beam indicated by two rays from the left strike adjacent planes separated by *d* at an angle θ_B. Scattered rays exit to the right also at an angle θ_B after reflecting from those planes. Constructive interference occurs when the path length difference indicated as *2p* is an integer number of wavelengths of the x-ray beam.

plane of θ_B as shown in Figure 6. The condition for constructive interference between adjacent planes in the crystal is (commonly known as Bragg's Law of x-ray diffraction(Bragg, 1913a)),

$$\lambda = 2d_{hkl}\sin\theta_B, \qquad \textbf{Equation 5}$$

where λ is the x-ray wavelength, θ_B is the Bragg angle of the incident and diffracted beam as measured away from the lattice planes and d_{hkl} is the lattice plane spacing. The indices associated with the lattice plane spacing identify the planes used in diffraction. An example of some silicon reflections, lattice spacings (d_{hkl}), and Bragg angles (θ_B) are provided in Table 2.

The diffraction from highly ordered crystals such as silicon obeys a diffraction law known as dynamical theory (Darwin, 1914b, a; Ewald, 1917, 1916b, a). Crystals whose lattice is completely uninterrupted over macroscopic distances (cm to m) are known as perfect crystals (Batterman and Cole, 1964). Silicon and a number of important semiconductor materials can be easily obtained as perfect crystals, primarily

due to manufacturing demands of the semiconductor industry for computer chips and imaging applications.

One of the characteristics of a highly ordered or perfect crystal is that diffraction of x-rays from lattice planes occurs over a narrow range of angles (Batterman and Cole, 1964; Azároff, 1974). Also, in that diffraction angle range, the reflectivity or the fraction of x-rays diffracted compared to the incident beam value can approach 1 or 100% which is high compared to other "normal" crystals; for example, NaCl or rock salt. Figure 7 is an example of the diffraction profile from a two crystal system. The first crystal is fixed in angle and this angle defines the x-ray beam energy which is diffracted from lattice planes within the crystal. The second crystal is now rocked in angle to give a reflectivity profile or "rocking curve" for this two crystal system (Azároff, 1974). Note that the horizontal axis is measured in microradians.

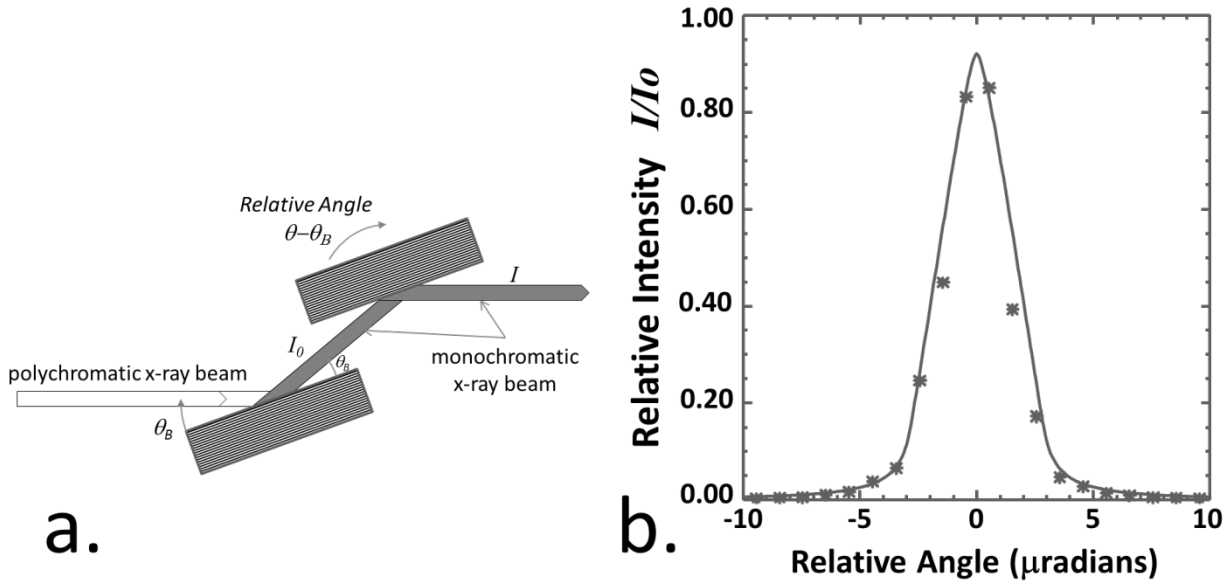

Figure 7 Diffraction from a two crystal system. The two crystal arrangement is shown in figure a. The first crystal is fixed and a monochromatic beam is selected from the polychromatic incident beam. The diffracted beam from the first crystal is then incident on the second matched crystal. Figure b shows the diffracted beam profile (rocking curve) as the second crystal is rocked near the Bragg angle. The curve shown is for a silicon (3,3,3) reflection at 18keV. The stars are measured relative intensity values (plot and measured data courtesy D. Chapman).

The typical DEI setup includes a third crystal as shown in Figure 4. In the DEI system, the monochromator is a double crystal system as shown above with a third analyzer crystal. In this arrangement, the two monochromator crystals are fixed in angle during imaging and the analyzer may

be optionally set at various offset angles to provide the desired image. The width of the reflection obtained by rocking the last crystal in a multiple matched crystal system is determined by the Darwin width (Als-Nielsen and McMorrow, 2001). The Darwin width determines the approximate full-width-at-half-maximum for a perfect crystal rocking curve. The Darwin width is,

$$\omega_D = \frac{2r_e \lambda d_{hkl}}{\pi V_C \cos\theta_B} \left|F_{hkl}\right|, \qquad \textbf{Equation 6}$$

where $\left|F_{hkl}\right|$ is the magnitude of the structure factor for the (h,k,l) reflection and Vc is the unit cell volume (0.160nm^3 for silicon). The other parameters have been defined in Equation 5.

Table 2 gives a few values for the lattice plane spacing, structure factor magnitudes and Darwin widths for 20 and 40keV.

			20keV			40keV		
(h,k,l)	d_{hkl} (nm)	$\left\|F_{hkl}\right\|$	θ_B (deg)	ω_D (μr)	$\frac{1}{(\rho_2-\rho_1)\frac{\partial t_2}{\partial z}}\frac{\Delta N}{N}\,REF$ (cm^3/g)	θ_B (deg)	ω_D (μr)	$\frac{1}{(\rho_2-\rho_1)\frac{\partial t_2}{\partial z}}\frac{\Delta N}{N}\,REF$ (cm^3/g)
(1,1,1)	0.314	61.0	5.67	14.03	0.037	2.81	6.99	0.019
(2,2,0)	0.192	68.6	9.28	9.74	0.054	4.64	4.82	0.027
(3,1,1)	0.164	44.5	10.89	5.41	0.098	5.44	2.67	0.049
(4,0,0)	0.136	57.4	13.18	5.85	0.091	6.53	2.87	0.046
(3,3,1)	0.125	39.1	14.38	3.67	0.146	7.16	1.79	0.073
(4,2,2)	0.111	50.3	16.21	4.24	0.127	8.02	2.06	0.064
(3,3,3)	0.105	33.7	17.25	2.69	0.202	8.54	1.30	0.101
(4,4,0)	0.096	44.1	18.85	3.27	0.168	9.28	1.57	0.084

Table 2 Lattice plane spacing, structure factor, Bragg angle, Darwin widths and refraction sensitivity at 20 and 40keV for a few selected silicon reflections.(Chapman, 2011)

As noted in Table 2, the width of the rocking curve is a function of the reflection used as well as the photon energy. Figure 8 shows this effect.

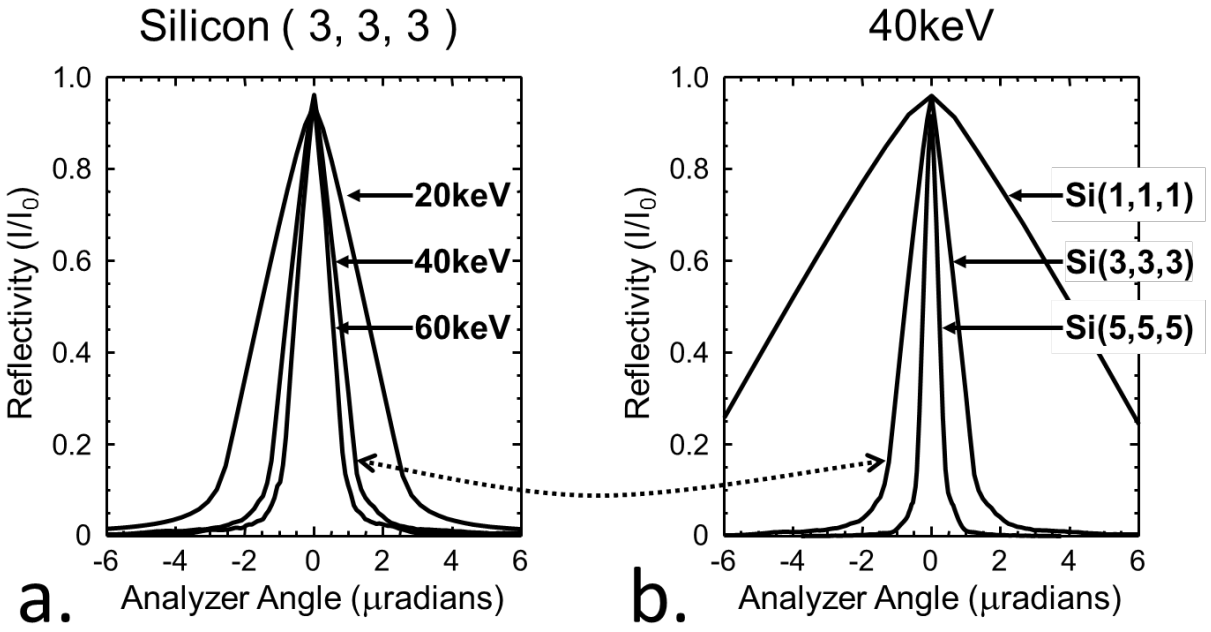

Figure 8 Rocking curves for silicon. Figure a shows the effect of increasing photon energy for the silicon (3,3,3) reflection. Figure b shows the effect of different reflections ((1,1,1), (3,3,3) & (5,5,5)) at a fixed photon energy of 40keV.(Chapman, 2011)

2.2.3 Imaging with an Analyzer Crystal

In a DEI system, the object being imaged is placed between two crystals with the detector placed after the last crystal which is referred to as the analyzer crystal. It should be noted that in a DEI system it is critical that all of the crystals have matching reflections or all using the same (h,k,l) and that all of the crystals be in a parallel arrangement. It is the analyzer rocking curve which provides two key roles in the

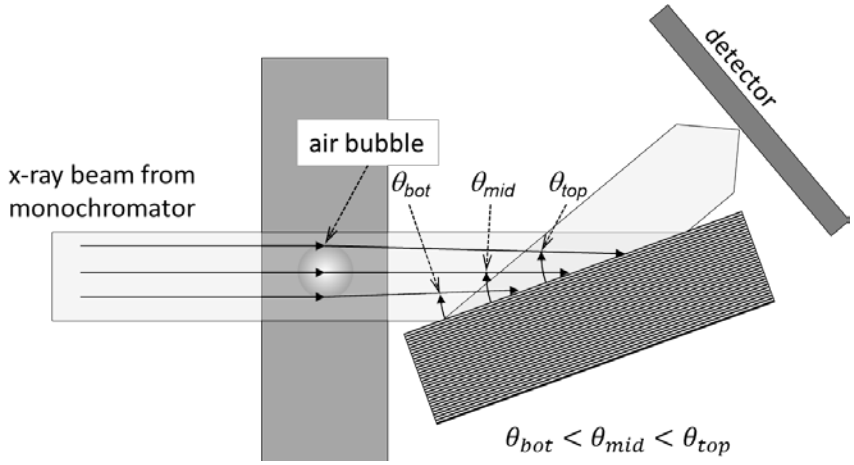

Figure 9 Effect of an air bubble on the path of x-rays at the top, middle and bottom of the bubble. Note that the angle the beams strikes the analyzer crystal is altered compared to the incident beam except for the middle beam. The bottom ray is at a shallower angle than the middle ray which is at a shallower angle than the top ray.

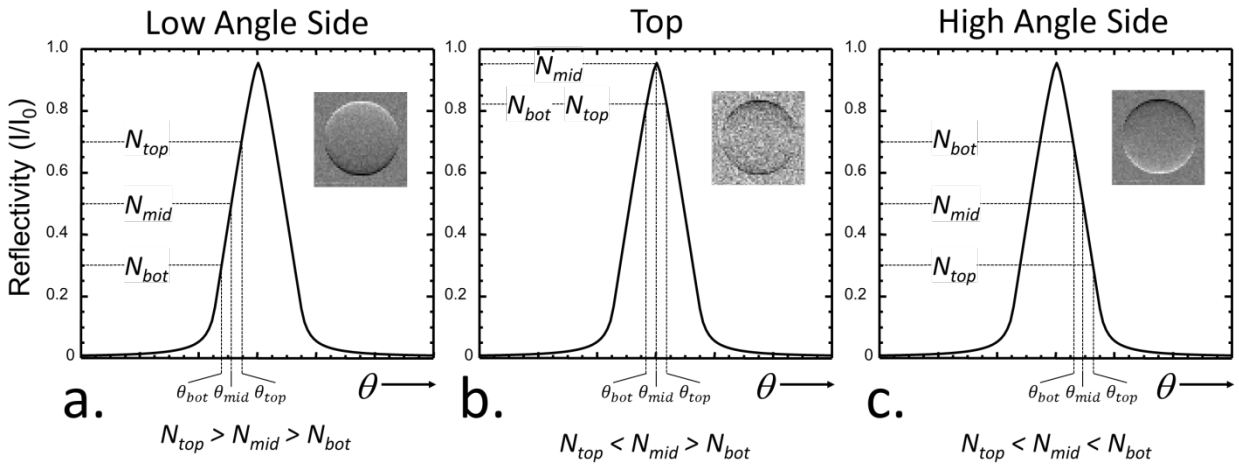

Figure 10 Appearance of air bubble with three analyzer settings. Figure a is with the analyzer set to the low angle side, figure b is with the analyzer set to the top and figure c is with the analyzer set to the high angle side. The image insets in each graph indicate how the bubble would appear in an image. (Chapman, 2011)

imaging process in the parallel crystal system. The steep slopes of the analyzer rocking curve can convert small angle variations into intensity variations. For example, Figure 9 shows schematically x-rays prepared by a monochromator striking an air bubble embedded in some material such as water. Since the air bubble has a higher refractive index compared to water, the bubble will act like a lens and focus the x-rays. Note that the path of the ray that strikes the middle of the bubble will be unaffected. The rays at the top of the bubble will strike the analyzer crystal at a slightly larger angle to the crystal while the rays at the bottom of the bubble will strike the analyzer at a slightly smaller angle. Normally, these angles are far too small to cause any noticeable deviation of the x-ray beam in a conventional x-ray imaging system. However, when they strike the analyzer crystal the difference in angle will alter the intensity detected after the analyzer. This effect is shown in Figure 10. This figure shows three different settings of the analyzer and the effect on the images with those analyzer settings. Figure a shows the analyzer set to the low angle side. The direct beam (without any object) will strike the analyzer on the low angle side of the rocking curve; at the ½ maximum point as shown in the figure. Now when the refraction from the bubble is included, the ray at the top of the bubble strikes the analyzer at a larger

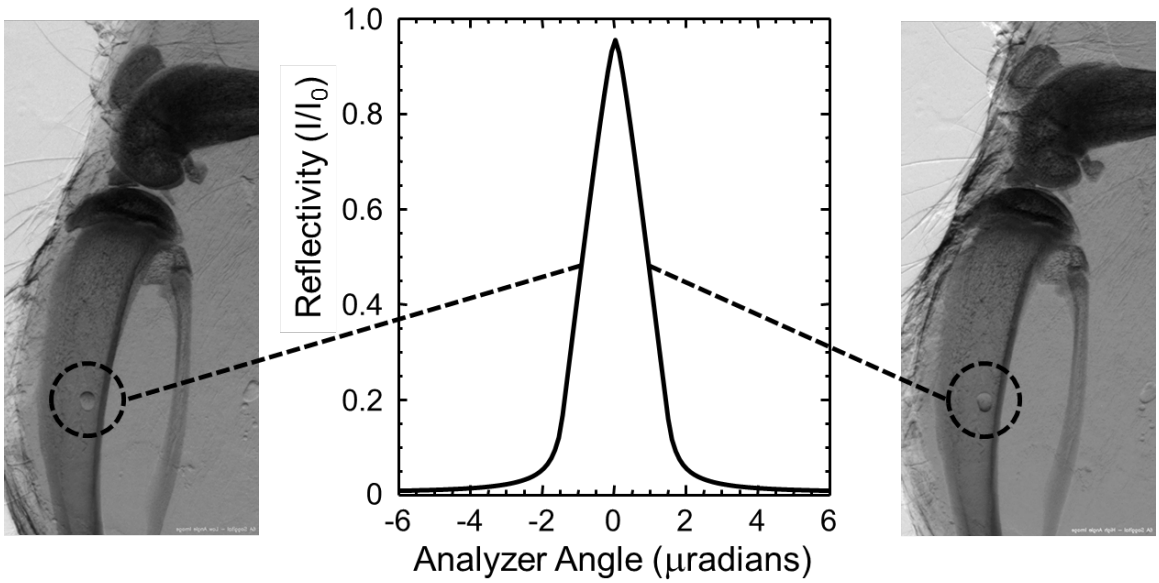

Figure 11 Example of sagittal images acquired on each side of the analyzer rocking curve of a rodent tibia-fibula. This image was chosen to illustrate refraction contrast on either side of the rocking curve because of the presence of an air bubble projected over the bone. The left image taken with the analyzer set on the low angle side (negative). The right image is taken on the high angle side (positive). Note the inversion of the shadow on an air bubble projected over the bone (circled region shown in both images). The images and rocking curve are for silicon (3,3,3) at 33keV.

angle and thus will translate to a higher reflectivity as shown in the figure while the bottom ray at a smaller angle will translate to a lower reflectivity. The small figure in the graph shows how the bubble might appear in an image under those conditions. There is a “white over black” shadow on the bubble

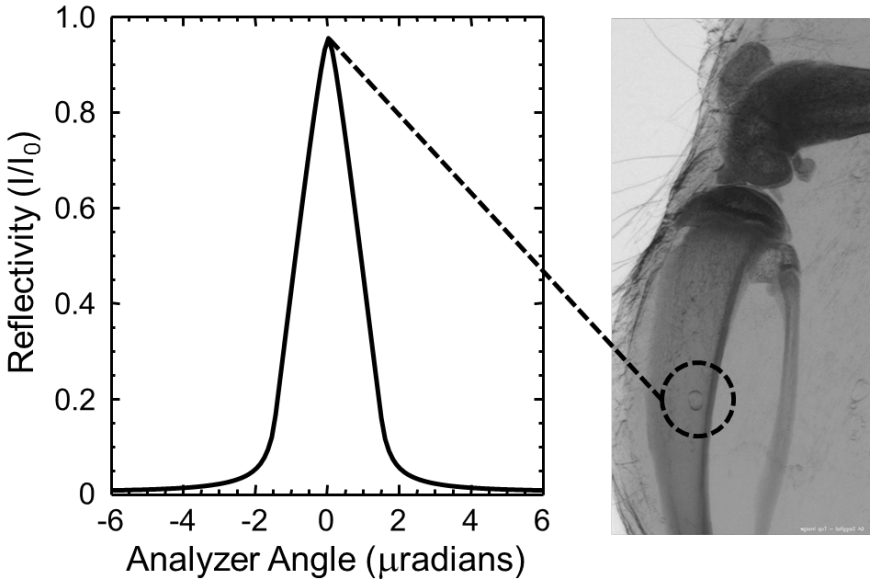

Figure 12 Example of an image taken at the top of the analyzer rocking curve (0 location on rocking curve). Note that the shadows on the bubble are now symmetric on top and bottom with lower intensity.

directly because of the refraction of the bubble. Figure c shows the analyzer set to the high angle side of the rocking curve. Now the slope of the curve is opposite and the relationship between the refraction angles and the detected intensities in an image are reversed. The top ray striking the analyzer now corresponds to a lower reflectivity and the bottom ray to a higher reflectivity. Thus, the bubble now has a “black over white” shadow. Figure b shows the situation where the analyzer has been set to the peak of reflectivity. In this condition, any un-deviated rays will be at maximum reflectivity. This occurs at the middle of the bubble. Now any ray that is not parallel to the incident beam will have lower reflectivity. For this reason, the top and bottom of the bubble has lower intensity.

Representations of these effects on samples from this thesis are shown in Figure 11 for images acquired on each side of the rocking curve. Figure 12 is an example of the same tissue as imaged with the top setting of the analyzer.

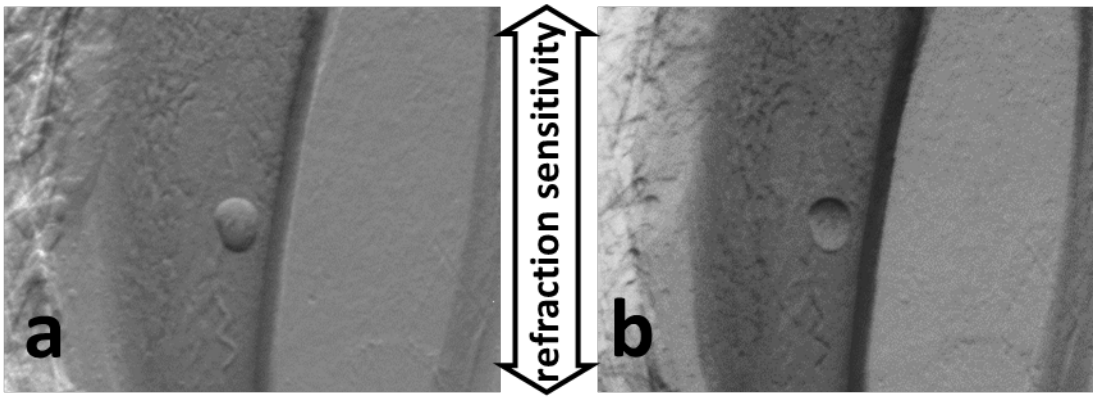

Figure 13 DEI image showing refraction contrast of an air bubble. Figure a is taken with the analyzer set to the low angle side of the rocking curve; b is on the high angle side. The arrow in the middle shows the refraction sensitive direction which is vertical in the figure as well as in the experimental setup. This figure further illustrates the directional effect of refraction contrast in a DEI system.

The shadows that appear on the DEI images shown thus far only occur on the top and bottom of refracting features of the object. This effect occurs because the DEI system has a direction in which it is sensitive to x-ray refraction. This direction in all synchrotron imaging systems is the vertical direction. Formally, the sensitive direction is parallel to the diffraction plane of the crystals perpendicular to the direction of the x-ray beam as it goes through the object. Figure 13 shows an enlarged image of the bubble in the sample image of Figure 11 to further emphasize the refractive sensitive direction effect on image contrast as indicated by the arrow.

The narrow angular width of the rocking curve also provides an extreme amount of scatter rejection at any setting relative to the incident beam. Since a typical analyzer rocking curve width is in the microradian angular range (see Table 2), scatter outside of the angular range is quite effectively rejected. Compare this with a typical anti-scatter grid of a conventional imaging system which rejects scatter on the degree angular range (Hendee and Ritenour, 2002). The increased ability to reject scatter with an analyzer is approximately 10,000 higher (1 degree = 17450 microradians). This enhanced scatter rejection gives rise to a high signal to noise for DEI as well as creating a new source of contrast from extreme scatter rejection commonly referred to as extinction contrast (Zhong *et al.*, 2000a). An example is shown in Figure 14. These two images were acquired under similar conditions. Both were

acquired at a synchrotron (BMIT bend magnet beamline at the CLS) with the same imaging energy (40keV) and detector (Photonic Science, XDR 90). The only difference is that Figure 14b is taken with an analyzer in place after the object and before the detector. The contrast settings of the two images are also the same. There are several bubbles in the mouse which can be seen over the abdomen of the animal in both images. In Figure 14b, those bubbles have dark shadows on the top and bottom side of the bubble indicating the image was taken near the top of the analyzer rocking curve (there is some slight misalignment from the peak or top position since the shadows are not completely symmetric – the

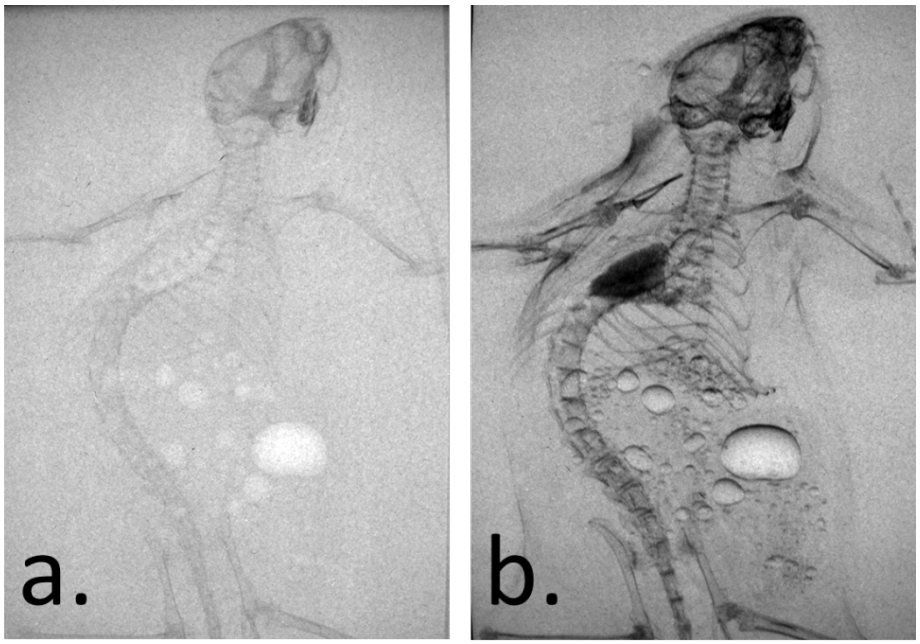

Figure 14 Images of a mouse. Figure a is a radiograph using the radiography setup shown in Figure 4a and Figure b is with the analyzer top setting using the DEI setup shown in Figure 4b. Both images are taken with the same detector and imaging conditions (40keV, (4,4,0) monochromator at the BMIT bend magnet beamline) (publicly supplied images courtesy BMIT)

top shadow is darker than the bottom). Note that the contrast for many structures in Figure b is higher than in Figure a. This is due in part to the enhanced contrast because of lack of Compton scatter from the object and in part due to the extreme scatter rejection providing contrast. In analyzing the bones, the part of the contrast from absorption is shown in Figure a; Figure b has significantly higher contrast. The trabecular structure of bone has refracted the x-rays multiple times which is then rejected by the analyzer crystal because the photon rays are outside the rocking curve in angle.

One obvious difference between the absorption and the diffraction image is the contrast generated by the lungs. The lungs are radiolucent in absorption radiography but in the DEI image the lungs have a positive contrast. This is because of the multiple refraction interfaces of the alveoli and connective tissue. This is a good example of what is commonly referred to as "extinction contrast" or "ultra-small angle scatter rejection contrast" (Zhong *et al.*, 2000a).

2.2.4 DEI Refraction and Apparent Absorption Analysis

The two images taken with the analyzer set to either side of the rocking curve can be used to create two images, one based on x-ray refraction effects (DEI refraction image, $\Delta\theta_{REF}$) and one based on what appears to be absorption (DEI apparent absorption image, N_{AABS}). Mathematically, these images are (Hayat, 2007; Chapman *et al.*, 1997),

$$N_{AABS} = \frac{N_H \frac{dR}{d\theta}(\theta_L) - N_L \frac{dR}{d\theta}(\theta_H)}{R(\theta_H)\frac{dR}{d\theta}(\theta_L) - R(\theta_L)\frac{dR}{d\theta}(\theta_H)}$$
$$\Delta\theta_{REF} = \frac{N_L R(\theta_H) - N_H R(\theta_L)}{N_H \frac{dR}{d\theta}(\theta_L) - N_L \frac{dR}{d\theta}(\theta_H)} \quad \textbf{Equation 7}$$

In this equation the subscripts, H and L, refer to images taken with the analyzer crystal set to the low and high angle settings as shown in Figure 11. Therefore, $N_{L,H}$ refers to images, $R(\theta_{L,H})$ the reflectivities, $\frac{dR}{d\theta}(\theta_{L,H})$ the slopes taken with the low and high analyzer settings respectively. Usually, the low and high analyzer settings are at the ½ maximum points on the rocking curve. Under these conditions ($R(\theta_L) = R(\theta_H) = \frac{1}{2}$; $\frac{dR}{d\theta}(\theta_L) \cong \frac{1}{\omega_D}$; $\frac{dR}{d\theta}(\theta_H) \cong -\frac{1}{\omega_D}$) the above equation becomes approximately (Zhong *et al.*, 2000a),

$$N_{AABS} \cong N_H + N_L$$
$$\Delta\theta_{REF} \cong \frac{\omega_D}{2}\frac{N_L - N_H}{N_L + N_H} \quad \textbf{Equation 8}$$

Equation 8 is used to obtain the refraction and apparent absorption images in this and other works since it is common practice to take images at the ½ reflectivity points.

An example of this analysis using the images from Figure 11 is shown in Figure 15.

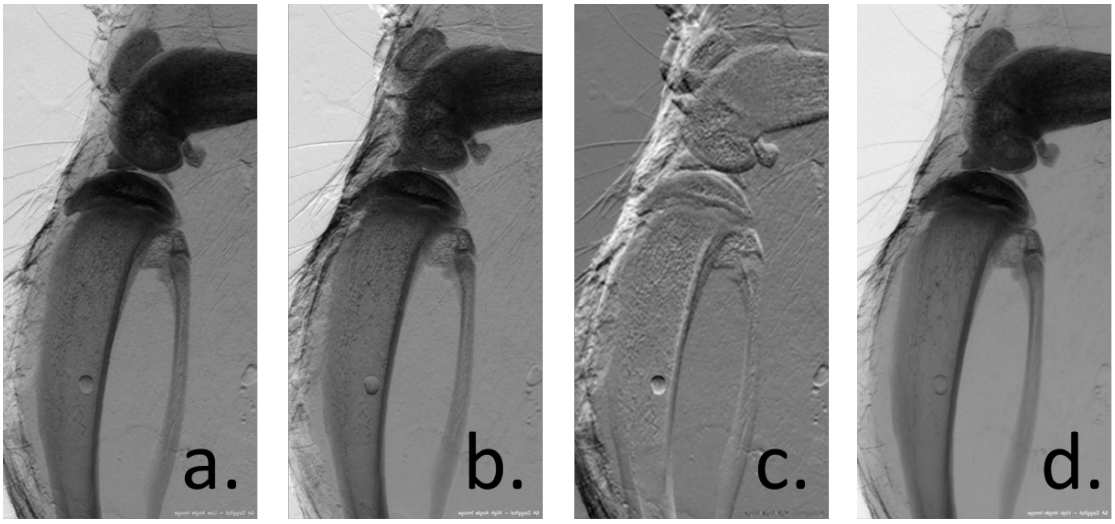

Figure 15 Example of the DEI Refraction and Apparent Absorption Analysis. Figure a is the sagittal image taken of a rat tibia – fibula with the low angle analyzer setting, figure b is with the high angle analyzer setting, figure c is the DEI Refraction Angle image and figure d is the DEI Apparent Absorption image.

2.2.5 Refraction Contrast

It is useful to determine the relationship between refraction and the observed contrast in an image. The equation given above for the refraction image of DEI does not relate image contrast refraction; just an algorithm to obtain the refraction image.

When x-rays penetrate an object, the change in measured intensity due to refraction is approximately (Hayat, 2007),

$$\frac{\Delta N}{N}_{REF} \cong \frac{\sin 2\theta_B}{\frac{4u}{V_C}\left|F_{hkl}\right|}\left(\rho_2 - \rho_1\right)\frac{\partial t_2}{\partial z}, \qquad \textbf{Equation 9}$$

where θ_B, the Bragg angle, $\left|F_{hkl}\right|$, the structure factor magnitude and V_C, the unit cell volume were defined previously. The quantity, *u*, is the nucleon mass ($1.66\text{x}10^{-24}$g). The mass density difference between the embedded object and the matrix material is $\rho_2 - \rho_1$ and the change in thickness of the

object along the sensitive direction is represented by $\frac{\partial t_2}{\partial z}$ (formally the gradient in embedded object thickness along the sensitive direction, z) (Zhong *et al.*, 2000a).

Since the density difference and gradient are properties of the object with the remainder of the values defined by the DEI imaging system, we define the refraction sensitivity as (Chapman, 2011),

$$\frac{1}{(\rho_2-\rho_1)\frac{\partial t_2}{\partial z}}\frac{\Delta N}{N}_{REF} \cong \frac{\sin 2\theta_B}{\frac{4u}{V_C}|F_{hkl}|}. \qquad \textbf{Equation 10}$$

The refraction sensitivity of Equation 10 is listed in Table 2 for a number of reflections and two imaging energies, 20 and 40keV. Note that the larger the value of the refraction sensitivity, the greater the contrast we obtain from refraction. This occurs for reflections with higher indices such as the (3,3,3) and (4,4,0). These reflections are commonly used for DEI as they have good sensitivity to refraction compared to lower index reflections. Higher index reflections will have even greater refraction sensitivity; however, high sensitivity also results in lower x-ray flux available for imaging. It is this

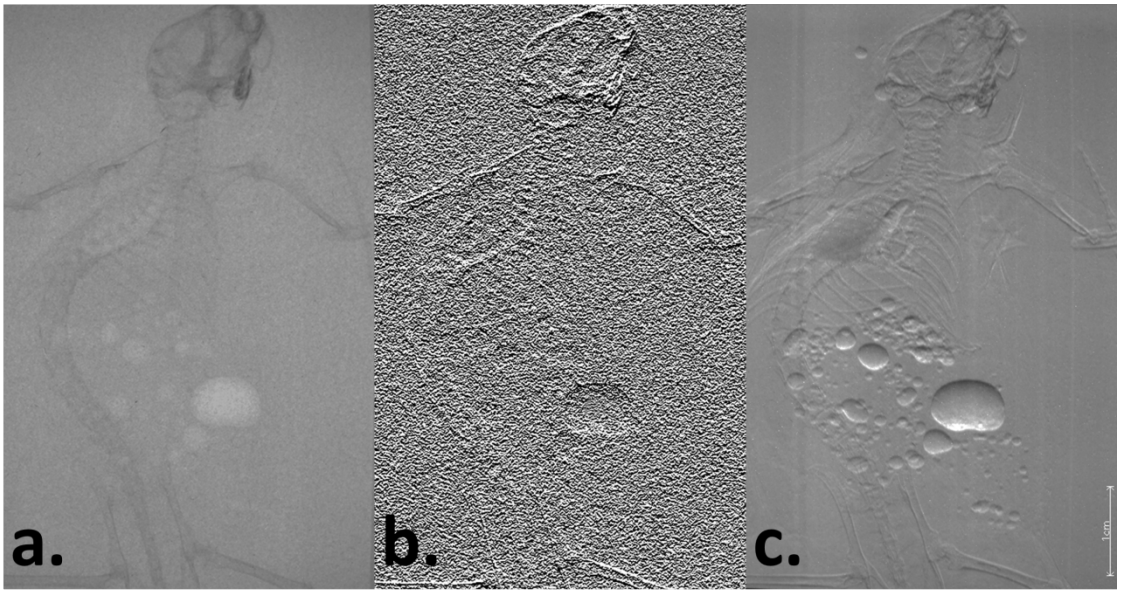

Figure 16 Example of creating a refraction type image from a radiograph. Figure a is a mouse radiograph taken on the BMIT beamline from Figure 13. Figure b is a gradient image created from a by a shift and subtract gradient method. Figure c is an image taken of the mouse with the analyzer crystal set to the side of the rocking curve. Note that the post processing of a radiograph to create a gradient image results in a noisier image that that acquired directly by DEI.

balance between sensitivity and x-ray flux which determines the best choice in a given imaging situation (Chapman, 2011).

2.2.5.1 Interpretation of Refraction or Gradient Images

The sensitivity of this imaging method to the gradient of the image is an important feature which requires some attention. If one were to simply take a radiograph of an object and then take the gradient of the image and completely avoid applying the DEI method, which is more complicated in comparison, it would show that there is a considerable amount of information lost in the image. As an example this process was done for an image set taken on the BMIT beamline (the mouse shown in Figure 14) and is shown again in Figure 16. Figure 16b is a mathematical gradient from Figure 16a by taking that image, shifting it vertically by one pixel and then subtracting that shifted image from the original. This process is equivalent to a gradient operation along the vertical direction. For comparison Figure 16c is a DEI image taken with the analyzer set to the side of the rocking curve. The gradient image in Figure 16b is noisy which is due to increased contrast (narrow contrast scale) settings to show the edge enhancement created by the gradient operation. The reason for the noisy gradient image has its origin is the relatively poor quality or low signal to noise of the original image because there was little absorption contrast present in that image. If the original image had more base line absorption contrast (which could be obtained by using lower imaging energy or a higher exposure), the radiation dose delivered to that object or tissue would be significantly higher than that of the DEI image to obtain an equivalent contrast above baseline noise. For the example given, the dose delivered to the mouse is the same for both the radiograph and the DEI image. The mouse image demonstrates one of the key features of the DEI process; the ability to derive contrast at higher imaging energies. If the same technical settings were applied to the absorption image, it would have decreased contrast because there would be little absorption contrast. Also, by using higher radiation energies with DEI there is less energy deposited into the object / tissue which results in a lower radiation tissue dose.

2.2.5.2 Quantification of DEI Images

Images acquired by the DEI process are interpreted in terms of refraction and absorption contrast. The absorption image can be analyzed in the same manner as a conventional radiograph. So far, the images shown are "intensity based" images, meaning that the pixel values are directly related to the number of photons arriving in that pixel. Most conventional radiographs are visualized as "negative logarithmic" relatively geographic representations of the object that was imaged. Historically in Diagnostic Radiology, this occurred naturally when x-ray film was exposed and then developed using photographic techniques (Haus and Cullinan, 1989). The images formed on the film (or negatives) are logarithmically related to the amount exposure on the film. If photons detected are interpreted as being transmitted through the object based on exponential attenuation (for example, see Figure 3), then the negative log will represent the projected attenuation, specifically (Hendee and Ritenour, 2002),

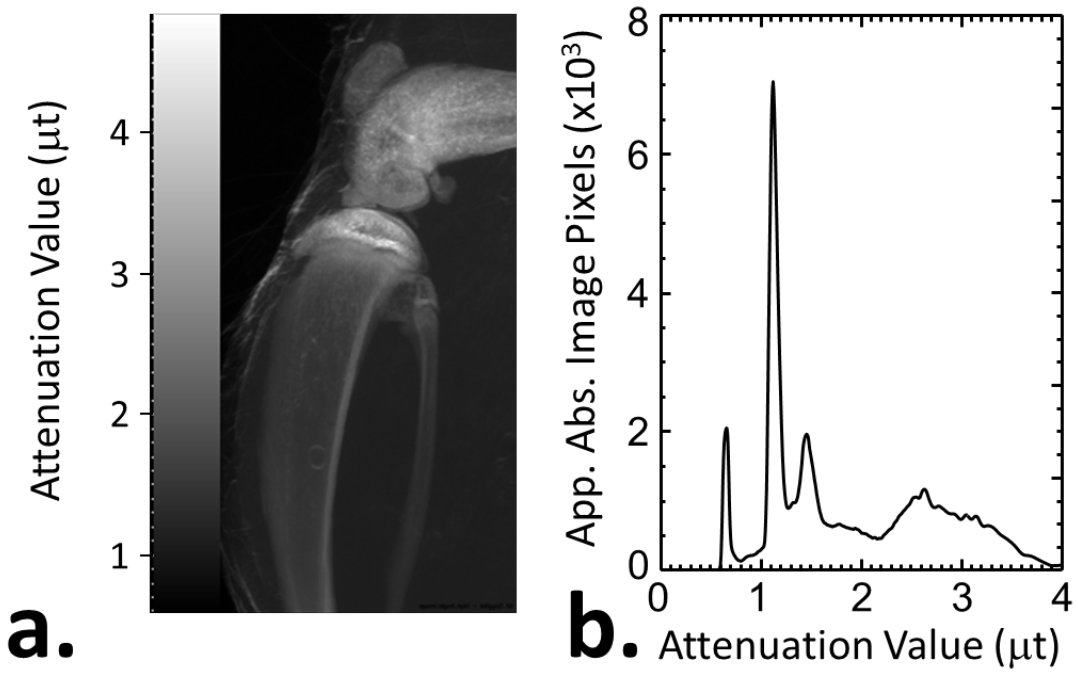

Figure 17 Negative logarithm version of DEI Apparent Absorption Image from Figure 15. Figure 17a shows the image with a gray-scale bar on the left to assist in interpreting the image values. Figure 17b show a histogram of the image showing the range of attenuation values along with the number of pixels that have that value.

$$N_{\det}(x,y) = N_0 e^{-\mu t(x,y)}$$
$$\mu t(x,y) = -\ln\left(\frac{N_{\det}(x,y)}{N_0}\right) \cdot \qquad \textbf{Equation 11}$$

Figure 17 shows the negative logarithm image from the DEI apparent absorption image shown in Figure 15. Figure 17a shows the image along with a gray-scale bar on the left. This shows the mapping between the gray-scale of the image and the value of projected attenuation (μt). The part of the bone in the sagittal plane with the most absorption or the densest bone is the epiphysis (around the knee). In this location the projected attenuation approaches a value of 4. The tissue is immersed in water so the minimum value of attenuation is now less than about 0.5. Figure 17b shows the pixel histogram values for the image in figure 17a. The histogram is a visual indication of the number of pixels that have an attenuation value as a function of that attenuation value. A peak in this plot indicates that there are many pixels that have similar or the same attenuation value. A uniform gray image would have a single peak at a single attenuation value with the height of that peak as the total number of pixels in the image. Inspection of figure 17b indicates that there are a variety of attenuation values in the image with some preferred values most likely corresponding to the water bath thickness.

The DEI refraction angle image has unique properties compared to either the conventional radiograph or DEI apparent absorption image. First, the refraction image is not an “intensity based image”. The pixel values are proportional to the refraction angle that the x-rays experience in traversing the object. As indicated in Equation 9 the refraction image is also proportional to the projected density gradient along a direction.

2.2.6Multiple Image Radiography Analysis

The DEI method allows only the derivation of refraction and apparent absorption images. The extraction of contrast from ultra-small angle scattering or extinction requires more than two images on each side of the rocking curve. The method of using more images and the analysis of them is commonly referred to as Multiple Image Radiography (MIR) (Wernick *et al.*, 2003; Pagot *et al.*, 2003; Oltulu *et al.*, 2003). In this thesis, only the DEI method is applied with two input images taken on opposite sides of the rocking curve (Chapman *et al.*, 1997).

In this work, the refraction image was of interest because it can potentially show subtle contrast

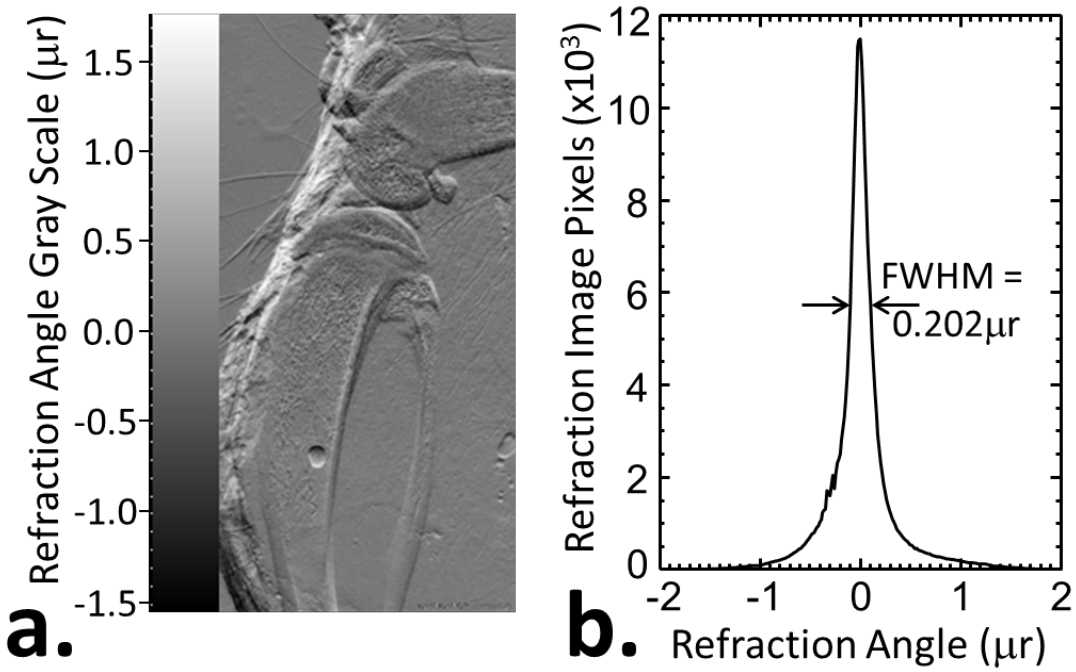

Figure 18 DEI Refraction Angle Image – same data set as in Figure 15. Figure 18a shows the image with a gray-scale bar on the left to assist in interpreting the image values. Figure 18b shows a histogram of the image demonstrating the range of attenuation values along with the number of pixels that have that value.

variations that would not be detectable in conventional absorption imaging. Each image has object contrast features that can be teased out either by enhancing the refraction contrast or the absorption contrast. As described above, in this project, the potential for refraction contrast was the focus.

2.3 Physeal Fractures

All long bones of a growing child consist of an epiphysis, physis (growth plate) and a metaphysis at each end of the diaphysis (shaft). This is demonstrated in Figure 19. In the embryo, the primary center of ossification is the diaphysis. It becomes the central shaft of the long bone by enlarging circumferentially by periosteal and membranous osseous tissue apposition. The secondary center of ossification is located in the epiphysis. The epiphysis is cartilaginous at birth and then undergoes central ossification and enlarges from a central nucleus. The longitudinal growth of long bones occurs at the epiphyseal plate which is the cartilaginous disc between the epiphysis and the metaphysis. Most long bones in mammals form via endochondral ossification. Endochondral ossification is the formation of bone tissue within and replacing cartilage. Once the bone has formed, endochondral ossification and growth of long bones occurs only at cartilaginous growth plates situated between a bony epiphysis and a bony diaphysis. Because of the malleability of the cartilage matrix it is possible to have proliferation of cartilage cells (chondroblasts) at the epiphyseal end of the growth plate and increasing maturation of the chondroblast cells (chondrocytes). The peak incidence of fractures involving the growth plate usually occurs during the growth spurt in both genders, usually at the time of puberty [8 to 13 years for girls and 10 to 15 years for boys] (Alexander, 1976). The growth at the physis is accompanied by four changes of the chondrocytes occurring in concert. There is an increased rate of cell division, increased length of replicating columns, increased number of columns and an increase in size of the cells (hypertrophy of cells). These proliferating and maturing cartilage cells secrete an intercellular matrix which provides tensile strength. When the cells are in a rapid growth phase, there is less matrix material in a given region relative to the cells and the probability of fracture is increased. The junction of the bony diaphysis and the growth plate is characterized by erosion of the cartilage by chondroclasts and the laying down of bone matrix by proliferating, invading bone-forming cells (osteoblasts). As long as there is a balance between cartilage formation and erosion and replacement with bone tissue at the metaphyseal end of the growth plate, the "bone" grows in length. However, when cartilage erosion and bone replacement occur faster than cartilage formation, then the growth plate disappears and the "bony" skeletal element can no longer increase in length. Physeal union may be defined as beginning

with the first mineralized bridge from the epiphyseal bone to the metaphyeal bone and ending with the complete disappearance of the cartilaginous physeal plate and its replacement with bone marrow (Haines, 1976). Most growth plates disappear or fuse during the teen years and when this occurs it is considered skeletal maturation.

Four types of growth disturbances have been described following fractures involving the growth plate(Hefti *et al.*, 1991). Overgrowth of the physis, decreased or arrested growth of the physis, growth in one part of the physis producing an angular deformity and asymmetric growth arrest due to a bone bridge. The most plausible explanation for the overgrowth of the physis is due to hyperemia related to fracture healing. This is the least common of the four post-traumatic features and when it does occur, it

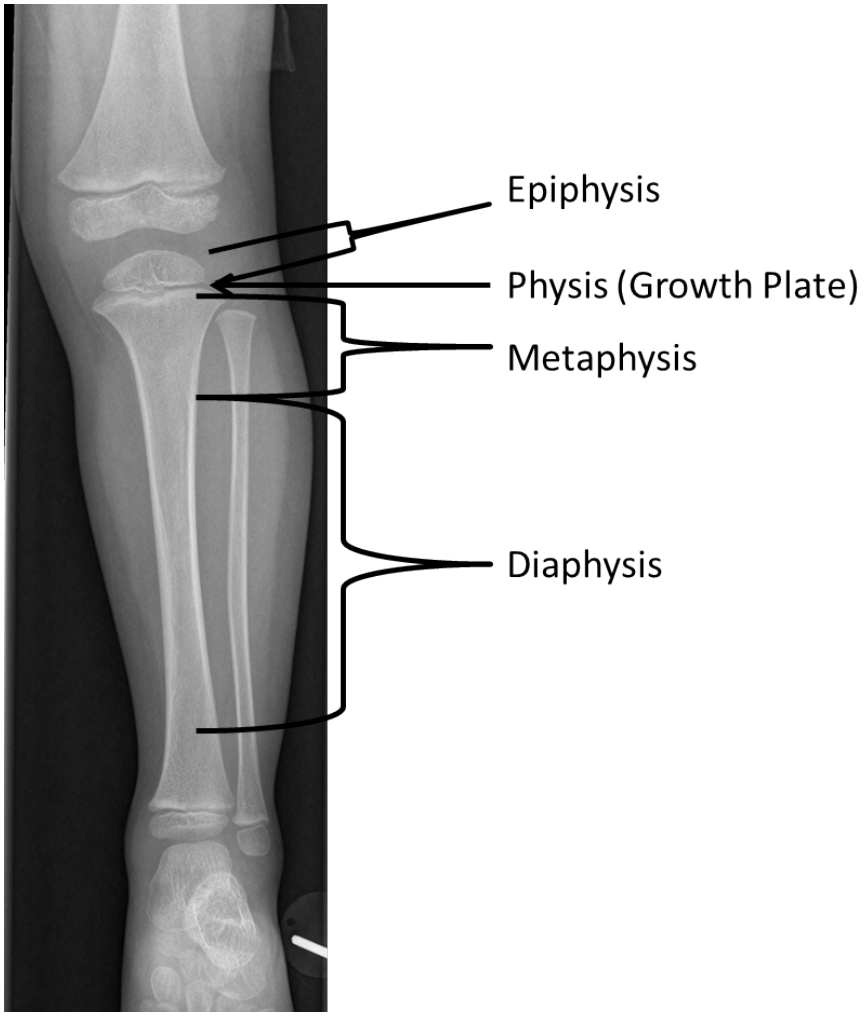

Figure 19 Clinical Radiograph of the Tibia and Fibula with notations indicating the epiphysis, physis, metaphysis and diaphysis.

is modest. The other features of growth arrest in one part or all the physeal plate is more common and often produces the most severe growth disturbances.

About 40% of boys and 25% of girls suffer a fracture before the age of 16; of these 14-27% are fractures through the physeal or growth plate (Williams, 2006). Of these physeal fractures approximately 25% result in premature closure, due to the formation of a bony bridge across the growth plate often resulting in shorter than normal bones (Barmada *et al.*, 2003).

Bone bridge formation appears to occur in response to an inflammatory response at the site of injury with inflammatory and mesenchymal cells infiltrating the fracture zone (Xian *et al.*, 2004; Chung *et al.*, 2006; Zhou *et al.*, 2004). Inflammatory cytokines promote expression of vascular endothelial cell growth factor (VEGF) in chondrocytes (Honorati *et al.*, 2004). Furthermore, soluble VEGF is necessary for growth of blood vessels into epiphyseal cartilage during the maturation of the physeal plate into metaphyseal bone when growth of the "bone" ceases (Maes *et al.*, 2004) and, hence, is likely responsible for infiltration of vascular elements into the fracture zone of the growth plate. Infiltrating blood vessels can arise from the coverings of the bone (the periosteum) or from the bone marrow: such blood vessels can bring cartilage destroying cells (chondroclasts) and bone forming cells (osteoblasts) into the fracture region.

3 Experiments

3.1 Method for Inducing Fractures

University of Saskatchewan Animal Research Ethics Board Protocol #20070092

University of Saskatchewan Biosaftey Permit #R-MED-11

Juvenile male Wistar rats were obtained in two separate batches. The first batch comprised 8 rats, each of which received a proximal tibial growth plate fracture at 5 weeks of age. The animals were individually anaesthetized with Isoflurane (5% induction/3% maintenance) inhalation. The left limb was isolated, shaved and cleaned with chlorohexidine and ethanol. Prior to the procedure 0.05mg/kg of subcutaneous Buprenorphine was administered for pre-operative analgesia. An incision was made in the skin lateral to the knee joint and the proximal tibial growth plate was visualized. Using both thumbs together and directing force medially (valgus stress) just below the knee joint, pressure was applied until a "pop" was felt and/or heard. The wound was then closed with 3.0 Vicry® (Ethicon). An attempt was made at placing a Plaster-of-Paris cast on the injured leg of all the rats, but in each case, the animal was able to slip off the cast within 8 hours. One of the rats (labelled 4A) managed to slip out of his cast almost immediately upon waking from anaesthesia – this was noticed, and his leg was recast immediately. His second cast lasted longer than 8 hours but was also eventually discarded by the rat by 20 hours post-operative. It was concluded that the casts were ineffective. Post-operative analgesia with subcutaneous Buprenorphine was given at 12 hours intervals for 3 days at tapered dosages of 0.04 mg/kg, 0.03 mg/kg, 0.02 mg/kg, and 0.01 mg/kg.

The rats were then euthanized by pericardial perfusion with normal saline followed by 10% phosphate buffered formalin while under Isoflurane anaesthesia. This was performed at 1, 2, 4 and 6 weeks post-operative to observe the different stages of healing. After tissue fixation, both lower limbs for each rat were dissected and immersed in plastic containers with 10% formalin. The rat lower limb specimens were subsequently labelled according to the following method:

2 rats – 1 week post fracture (specimens 1a and 1b)

2 rats – 2 weeks post fracture (specimens 2a and 2b)

2 rats – 4 weeks post fracture (specimens 4a and 4b)

2 rats – 6 weeks post fracture (specimens 6a and 6b)

Total of 8 rats – first batch

The second batch of rats received the induced fracture at 5 weeks of age. There were 12 rats in the second batch. It was decided that, from the earlier experience, a reproducible fracture could likely be made by palpating the knee joint, placing one thumb at the knee and the other just inferior to the joint, at the proximal tibia. Valgus force was then applied in a similar fashion to the first batch until a "pop" was felt and/or heard. No incision was made prior to the procedure on this second batch of animals. From prior experience and the apparent ineffectiveness of casts, no casts were placed on this second batch. The anaesthesia and pre- and post-op analgesia were identical to that of the first batch.

These rats were then euthanized and tissue fixated using the same protocol as the first batch. The lower limbs were dissected, and specimens labelled similarly to the first batch, and euthanized at the following time points.

3 rats – 1 week post fracture (specimen 1a, 1b and 1c)

3 rats – 2 weeks post fracture (specimen 2a, 2b and 2c)

3 rats – 4 weeks post fracture (specimen 4a, 4b and 4c)

3 rats – 6 weeks post fracture (specimen 6a, 6b and 6c)

Total of 12 rats - second batch.

3.2 Imaging Methods

DEI was performed at three facilities: 1) the National Synchrotron Light Source at Brookhaven National Laboratory using the X15A Imaging beamline (October 2008 and April 2009), 2) Nesch, LLC, Crown Point, IN using a laboratory based DEI system (Nesch *et al.*, 2009) (October 2008 to March 2009), and 3) the Biomedical Imaging and Therapy bend magnet beamline at the Canadian Light Source (December 2008).

Additionally, micro-computed tomographic (micro-CT) images were obtained using a SkyScan 1172 micro-CT system (Kontich, Belgium) from Dr. Cooper's laboratory at the University of Saskatchewan. The images were reconstructed to a 10 micron voxel size (10μm x 10μm x 10μm). The images acquired from this laboratory based system were for correlative purposes.

The specimens (First Batch) were shipped to Brookhaven National Laboratory where imaging experiments were carried out at the National Synchrotron Light Source X15A Imaging beamline. This facility has a dedicated DEI setup with a wide range of imaging energies. The experiments were performed near 33keV using a silicon (1,1,1) monochromator and analyzer setting.

The (h,k,l) are the lattice planes of the crystal used to collimate and analyze the x-ray beam. For our purposes the (3,3,3) has roughly five times higher sensitivity to refraction effects than the (1,1,1) reflection. The (1,1,1) was chosen for the CT measurements due to a reduced sensitivity to mechanical and thermal effects during the prolonged acquisition time (typically one hour per CT scan) as opposed to the few minutes required for a projection image.

The first batch specimens were also imaged on a x-ray tube based DEI system being developed by Nesch, LLC. This system utilizes a Ag anode x-ray tube (nominally 22keV imaging energy) also using Si (3,3,3)

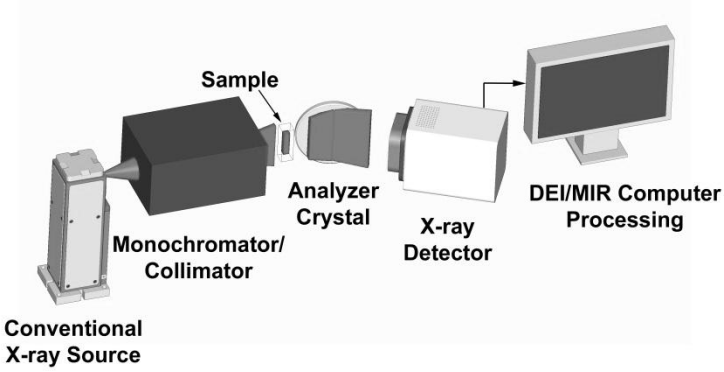

Figure 20 Schematic layout of the Nesch DEI Small Animal System which is based on a conventional x-ray tube operating at the Ag K alpha line near 22keV.

crystals for the monochromator – analyzer. A schematic layout of that system is shown in figure 20. This system has a single frame field of view of approximately 12mm X 60mm.

The second batch of specimens was kept for imaging at the Biomedical Imaging and Therapy (BMIT) bend magnet beamline at the Canadian Light Source The imaging energy was 41keV also using the Si (3,3,3) reflection for the monochromator and analyzer.

Specimens of the second batch were also imaged using the SkyScan micro-CT system. The images acquired by this system develop contrast based on absorption, not the DEI effect.

3.2.1.1 Projection Images

Projection DEI images were taken with various analyzer settings. Images taken with the analyzer set to +/- the full width half maximum points of the rocking curve can be used to determine independent refraction and apparent absorption images. Other images taken with that analyzer at the peak give maximum contrast due to rejection of ultra-small angle scattering. Images taken with the analyzer farther from the peak develop contrast from extreme refraction and acceptance of ultra-small angle scattering.

The acute flexed position of the knee of the specimens gave us some trouble in positioning the specimen in the coronal plane. Initially sagittal images were obtained at Brookhaven, then coronal images were attempted once BMIT was operational. Once the images were acquired, it became obvious that the visibility of the fracture was similar to the visibility of the growth plate itself and that our attention should actually be directed to improving imaging techniques rather than visualize each fracture pattern. The ability of DEI to detect the very tiny structures would not be better than conventional imaging including conventional CT and MRI. However the understanding of refraction images and finding its potential would be very valuable.

3.2.2 Computed Tomography

Selected specimens were subsequently imaged in a computed tomography mode. As noted earlier, the imaging energy remained at 33keV, however, the monochromator and analyzer was set to the (1,1,1) reflection to reduce sensitivity to thermal and mechanical vibration. Additionally, the wider reflectivity curve also reduced contrast to ultra-small angle scattering and thus improved the reconstruction of the images.

Images were acquired at 2000 angles (0.18 degree per rotation step) for three analyzer settings of -4.5, 0, and +4.5 microradians. Projection images were acquired at each rotation angle and analyzer setting

over the beam size of ~1.5 mm vertical x 40mm horizontal. The pixel size of the detector was 30 microns. The detector was a Photonic Science XDI VHR 100 with a maximum field of view of 75mm x 50mm. The long axis of the limb was arranged to be nearly parallel to the CT rotation axis.

The DEI-CT (Dilmanian *et al.*, 2000) process develops images similar to the projection DEI process. However, it employs methods common to the computed tomography to produce axial images based on projection images taken as the object is rotated about an axis. The reconstruction then occurs for a plane perpendicular to the rotation axis. The raw images acquired in the DEI process are a mixture of attenuation and refraction. Since the absorption CT process involves a non-linear operation (a logarithm) to arrive at the linear attenuation and thickness coefficients, the refraction and attenuation parts must be separated first prior to reconstruction. The refraction image is "linear" so it can be reconstructed directly and the apparent absorption image must have the negative logarithm taken prior to reconstruction.

With this arrangement a reconstruction of a 1.5mm region along the limb could be done. Extended coverage of the limb was done by vertically translating the limb in 1.2 mm increments. The overlap region ensured that the reconstruction could be stitched together seamlessly.

A diagram illustrating the image to CT reconstruction process is shown in Figure 21. This indicates the process used to take projection images at a specific analyzer location through the reconstruction process to axial images using a filter backprojection algorithm.

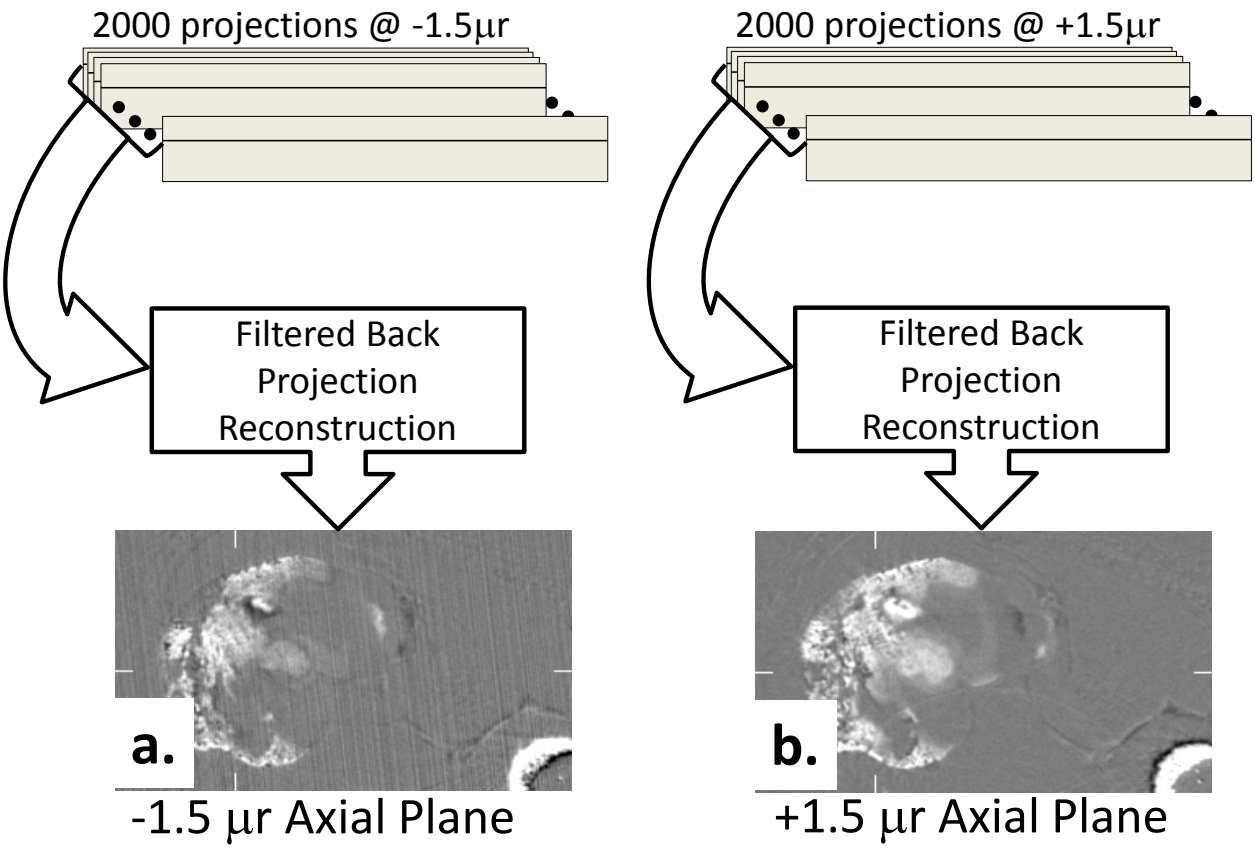

Figure 21 The process taking the 2000 projection images as the object (proximal tibia in the axial plane) is rotated 180 degrees to reconstructed axial planes of the object. Figure a is for images at -1.5microradians, b is for images at +1.5 microradians analyzer setting.

The process to reconstruct the DEI refraction and apparent absorption images requires that the DEI algorithm be applied prior to the filtered backprojection reconstruction. This process is illustrated in Figure 22.

An example of imaging the one week post-fracture specimen is shown in Figure 23. This figure shows three orthogonal views (axial, coronal, and sagittal) through the proximal tibia. These views are shown for the -4.5, 0, and +4.5 microradian analyzer setting.

The -4.5 and +4.5 analyzer images can be broken into refraction and apparent absorption images. This is shown in figure 4 for the same data set as in Figure 23.

These images provided more detail, both of the fracture and of the growth plate. The dark and light band along the metaphyseal edge at the zone of provisional calcification could be easily identified within the growth plate. The fracture edge was sharp because of the edge enhancement effect. However the time required to acquire this data set took two days and only one specimen was completely scanned.

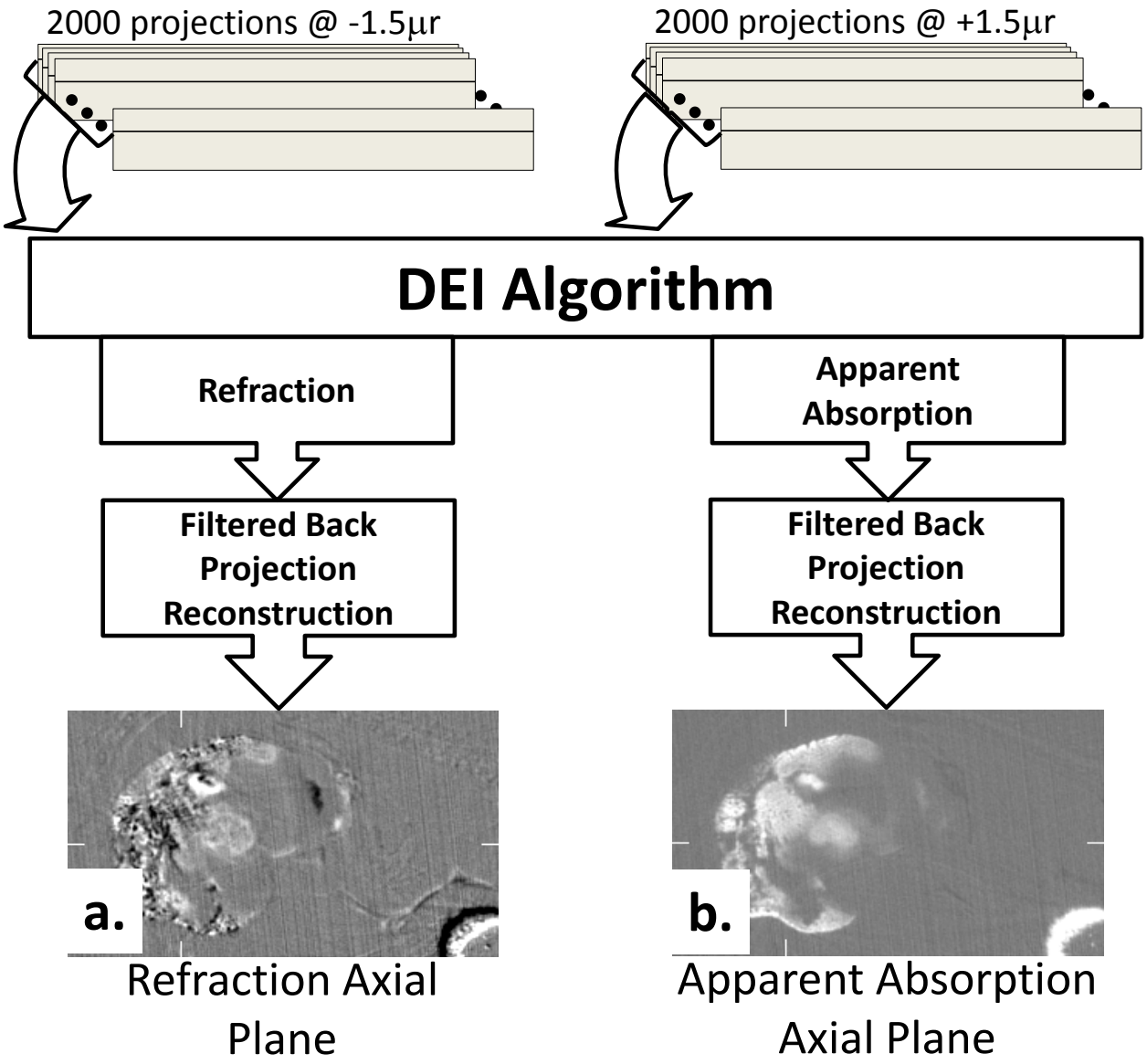

Figure 22 The process to produce DEI refraction and apparent absorption images in the axial plane (proximal tibia) from combining images taken on each side of the rocking curve. Figure a show the reconstructed refraction angle image and b shows the apparent absorption image.

4 Results

4.1 Synchrotron Projection Imaging Data (First Batch – Brookhaven)

Figure 23 shows a composite of images acquired with the analyzer set relative to the peak location at -1.5 microradians (row a), 0 microradians or at peak (row b), +1.5 microradians (row c) and at +3 microradians (row d). The harvested specimens are shown in post-fracture time order of 1 week (column 1), 2 weeks (column 2), 4 weeks (column 3) and 6 weeks (column 4).

Referencing Figure 23, the undulating surface of the growth plate in addition to the volume of tissue interfaces that the photons interact with (refraction) in the single plane make the interpretation of the images difficult. Each specimen is slightly different but the detail of each image is less than optimal due to multiple refractions occurring through the tissue. There are multiple dark and light linear structures that grossly resemble an edge enhanced absorption image, but the correlation of the image contrast with the object is not intuitive. There are a considerable number of linear contrast markings that probably do not represent the actual structure in the object due to “refraction artefact”.

The more the analyzer is moved from the peak or 0μr setting, the more refraction contrast we are able to see. This effect can be seen by looking at the bubble in Figure 23, 6 week column, left side. The bubble has been indicated with a circle. However, refraction has little effect on visualizing the fracture due to the specimen orientation in this image set.

In related work done at the CLS over the same time period as the results shown (Cooper *et al.*, 2010) it was realized that the anisotropic orientation of the bone trabeculae (refraction interfaces) has a pronounced effect on appearance of the images depending on the relationship of the major trabeculae relative to the DEI sensitive direction (vertical at the synchrotron).

The orientation of the bone trabeculae and the growth plate relative to the plane of refraction (which is parallel to the ground in synchrotron DEI systems) changes the image contrast. Tissue interfaces that are parallel to the plane of refraction demonstrate strong refraction contrast where tissue interfaces perpendicular to plane of refraction do not demonstrate any refraction contrast.

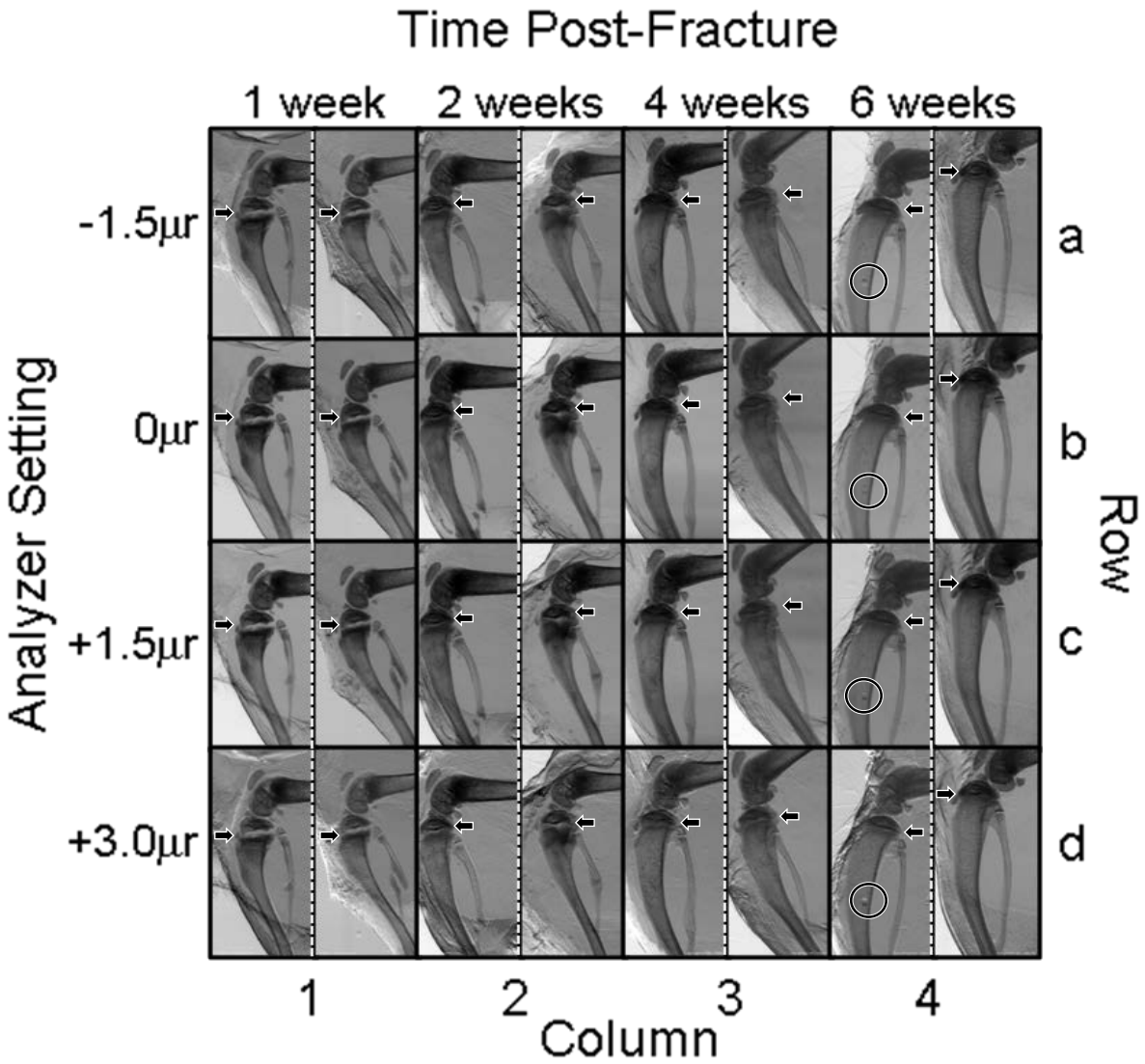

Figure 23 Projection images of two juvenile rat proximal tibia growth plate fracture specimens at various times post-fracture (column 1: 1 week, col. 2: 2 weeks, col. 3: 4 weeks & col: 4: 6 weeks – two specimens each for box) and analyzer settings (row a: -1.5mr, row b: 0mr, row c: +1.5mr & row d: +3.0mr). In each box the left image is specimen A and the right image is specimen B. The specimens where imaged in the sagittal plane because of the difficulty in holding the specimens in the coronal plane, which would have demonstrated the fracture. The arrow indicates the growth plate of the proximal tibia. The circles highlight an incidental bubble whose refraction contrast varies with analyzer setting. The fracture of the metaphysis is in-plane and cannot be visualized. This figure's purpose is to provide a general sense of the imaging appearance of DEI.

4.2 Synchrotron Computed Tomography Data (First Batch – Brookhaven)

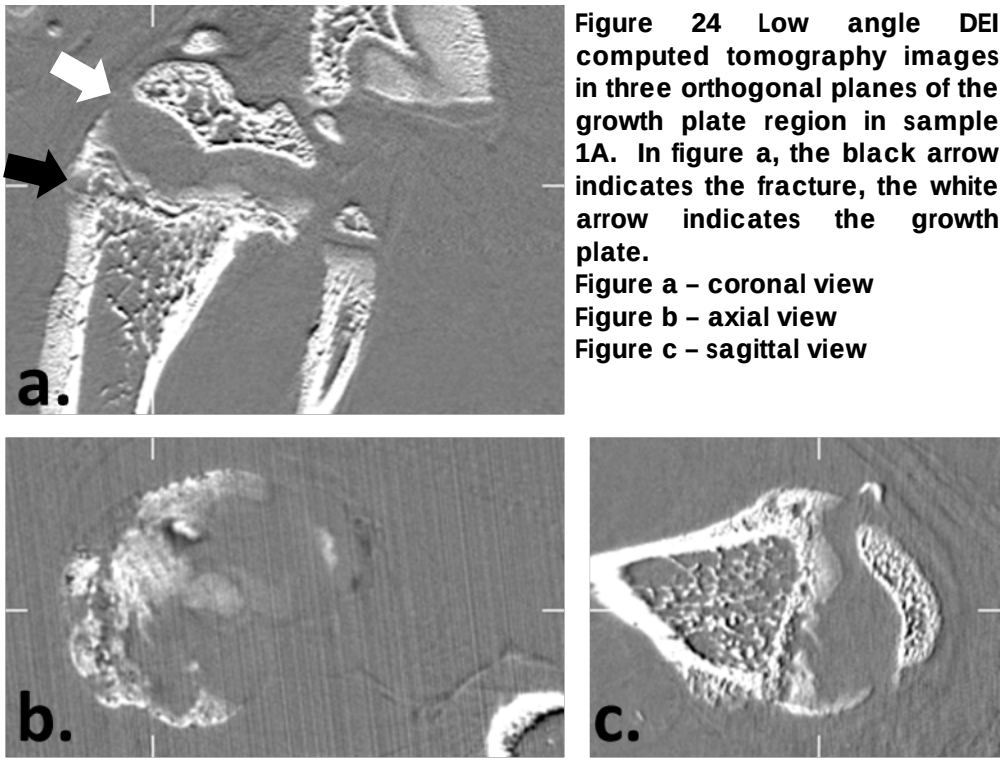

Figure 24 Low angle DEI computed tomography images in three orthogonal planes of the growth plate region in sample 1A. In figure a, the black arrow indicates the fracture, the white arrow indicates the growth plate.
Figure a – coronal view
Figure b – axial view
Figure c – sagittal view

Specimen 1A – fractured left leg was imaged at the NSLS in October 2008. Due to some technical difficulties and the time required to get the full data set (over the course of two days) only one specimen was imaged. One day was used for projection imaging described in section 4.1. The remainder was reserved for CT imaging. Each CT data set would normally require 4 to 6 hours of scan time. However, there were problems in reliably triggering image acquisition in the detector which was not resolved during the experiment. Several CT image sets were attempted; only one was successful. The CT images were acquired using the Si (1,1,1) in the monochromator – analyzer system at 33 keV. The CT set comprised 2000 projection angles in 0.18 degree increments. A dedicated filtered back projection algorithm was used to reconstruct the axial plane from the 2000 projections. A single rotation of the object covered a depth of 3mm slice. The detector had a pixel size of approximately 30microns (Photonic Science VHR-XDR 100).

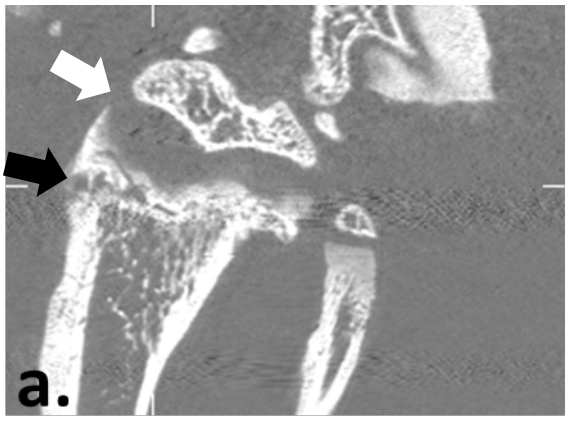

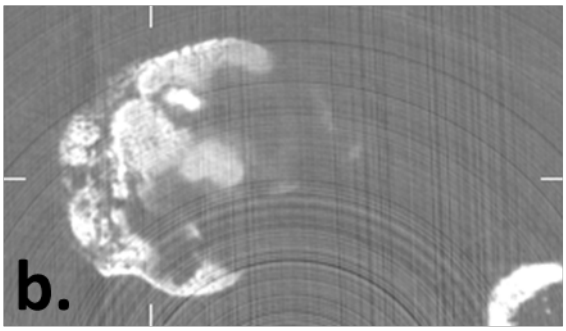

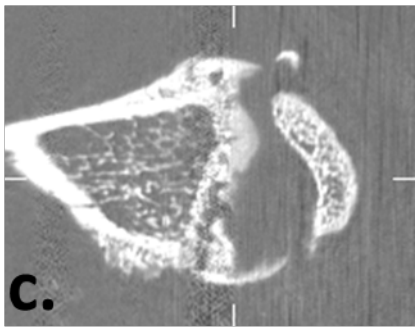

Figure 25 Analyzer top setting DEI computed tomography images of the 1A specimen showing the same region as in the previous figure. In figure a, the black arrow indicates the fracture, the white arrow indicates the growth plate.
Figure a – coronal view
Figure b - axial view
Figure c – sagittal view

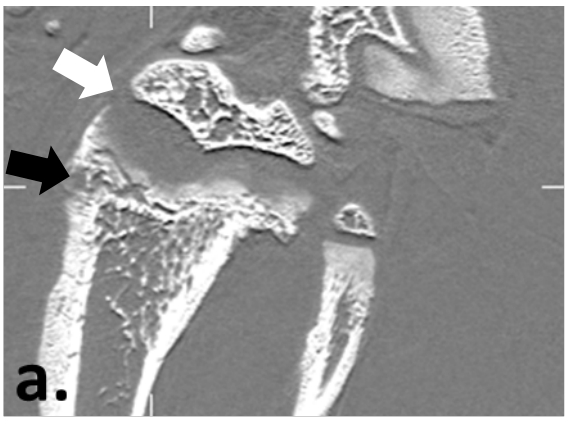

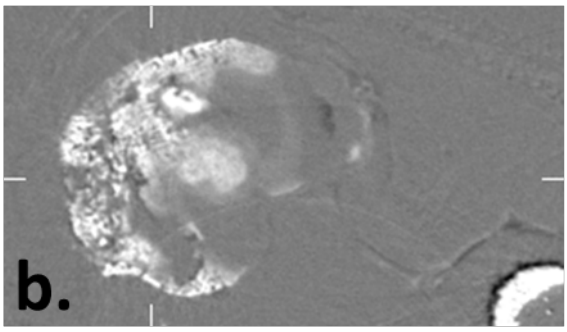

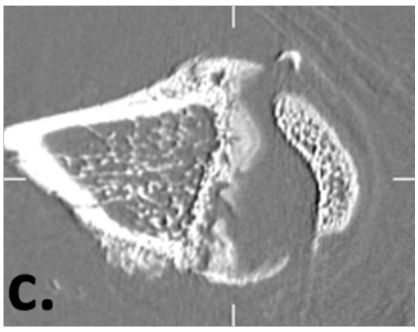

Figure 26 High angle DEI computed tomography images of the 1A specimen showing the same region as in the previous figure. In figure a, the black arrow indicates the fracture, the white arrow indicates the growth plate.
Figure a – coronal view
Figure b – axial view
Figure c – sagittal view

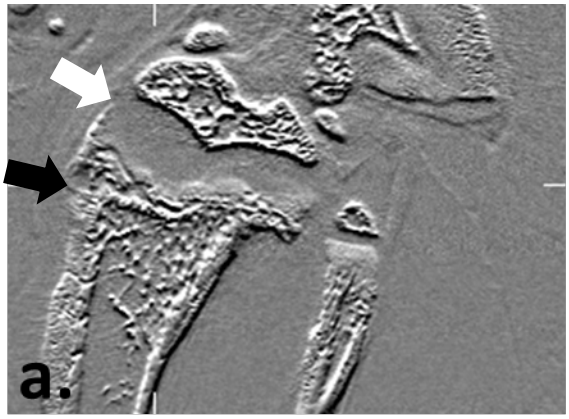

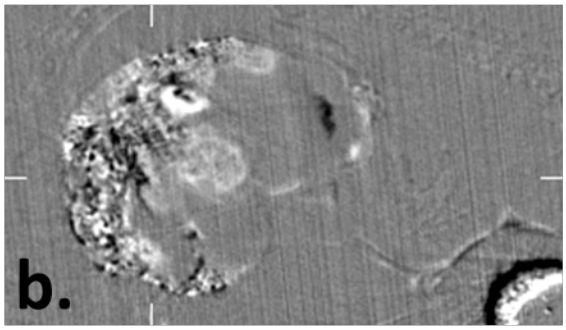

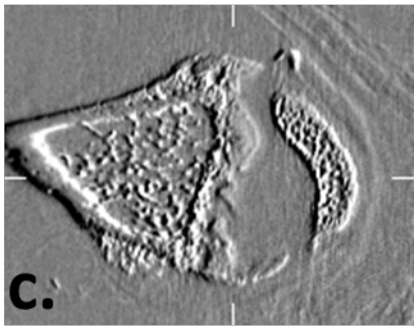

Figure 28 Refraction DEI computed tomography images of the 1A specimen showing the same region as in the previous figure. In figure a, the black arrow indicates the fracture, the white arrow indicates the growth plate.
Figure a – coronal image
Figure b – axial image
Figure c – sagittal image

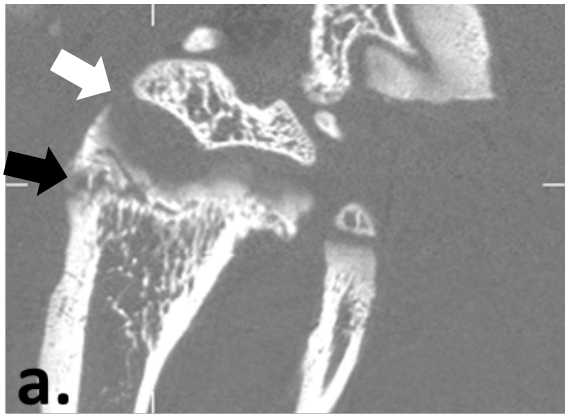

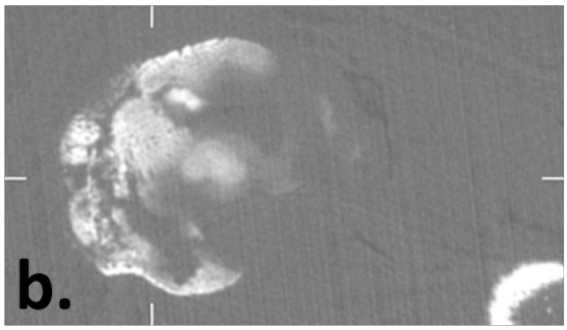

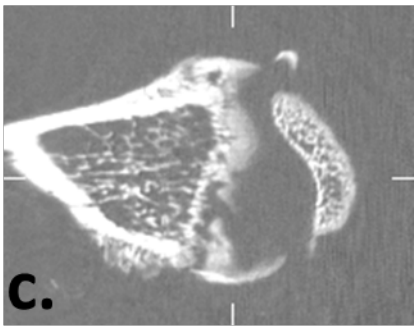

Figure 27 Apparent Absorption DEI computed tomography images of the 1A specimen showing the same region as in the previous figure. In figure a, the black arrow indicates the fracture, the white arrow indicates the growth plate.
Figure a – coronal view
Figure b – axial view
Figure c – sagittal view

Examples of the CT images are shown in Figure 24 through Figure 28. The cross sections shown are orthogonal views through the growth plate region. In all figures (a) is the coronal view, (b) the axial view and (c) the sagittal view. The CT data that was acquired was the low angle image set (Figure 24), the analyzer top image set (Figure 25) and the high angle image set (Figure 26). In all of the coronal views, the metaphyseal fracture is indicated with a black arrow and the growth plate is indicated by a white arrow.

The refraction (Figure 27) and apparent absorption (Figure 28) images sets are derived from the low and high angle sets using the DEI algorithm.

The orientation of the object relative to the refraction angle of the system still has an effect in that the tissue interfaces parallel to the refraction plane will demonstrate strong refraction contrast whereas the interfaces perpendicular will not demonstrate any refraction contrast. However, the object needs to spin to perform CT using synchrotron light (due to the fixed source of radiation). Currently the technical limitations only allow the object to spin in an orientation perpendicular to the refraction plane.

In our specimen, we are able to visualize the principal linear interfaces between the bone and cartilage of the growth plate, but any vertical bone spicules or columnar ossifications, if present, within the cartilage are not visualized. On a larger scale, the bony trabecular pattern of the metaphysis as it approaches the growth plate on the refraction images is largely lost with a mottled appearance across the metaphysis. When the interface is orientated obliquely or a 45 degrees, there is a “shift” of the refraction contrast. The dark and light bands are produced vertically, but because of the orientation of the structure it gives the illusion of a lateral shift. The fracture through the metaphysis in our specimen is in fact somewhat less conspicuous on the refraction image compared to the absorption image and this is again primarily due to the direction of refraction contrast. When the two bone-fracture interfaces becomes close together, the dark and light band slightly superimpose over the area of the interface itself, as seen on the absorption image. This may in fact indicate there is an inherent limit to the refraction contrast resolution.

The primary goal of visualizing tiny structures that will demonstrate refraction contrast that do not have enough mass to produce absorption contrast may still be possible. In our current project, this is unlikely due to the inability of the system to produce the sufficient absorption contrast, which is expected, but some of the refraction contrast probably is not apparent due to the orientation of the object.

Figure 29 Sagittal DEI images the rat tibia – fibula 1A specimen acquired with the Nesch laboratory based system. Figure a is an image acquired at the analyzer peak, figure b is an extinction image and figure c is a refraction image.

4.3 Laboratory Based Projection Imaging Data (First Batch - Nesch, LLC)

Some of the images of the 1A specimen (first batch) acquired with the Nesch system are shown in Figure 29. These images were acquired at approximately 22 keV using the Si (3,3,3) monochromator – analyzer settings. The images took approximately one day to acquire.

The images produced in this system were planar images using a low energy conventional stationary anode x-ray tube. The images produced are similar in appearance to planar synchrotron images, but with less signal to noise due to low photon flux. The refraction contrast is visible, similar to the

synchrotron produced images but the refraction plane of the system is vertical. As a result, the refraction contrast is in an orthogonal plane compared to the synchrotron based images. The detail remains limited by the limitations of the system however the potential to perform DEI in a laboratory using a conventional x-ray tube may provide some additional opportunities further explored in the discussion.

4.4 Synchrotron Projection Data (Second Batch – BMIT / CLS)

The Biomedical Imaging and Therapy beamline was being commissioned during the data collection phase of the growth plate fracture project. Images of one of the tibia – fibula fracture specimens were acquired to compare with results from the National Synchrotron Light Source DEI system, the laboratory

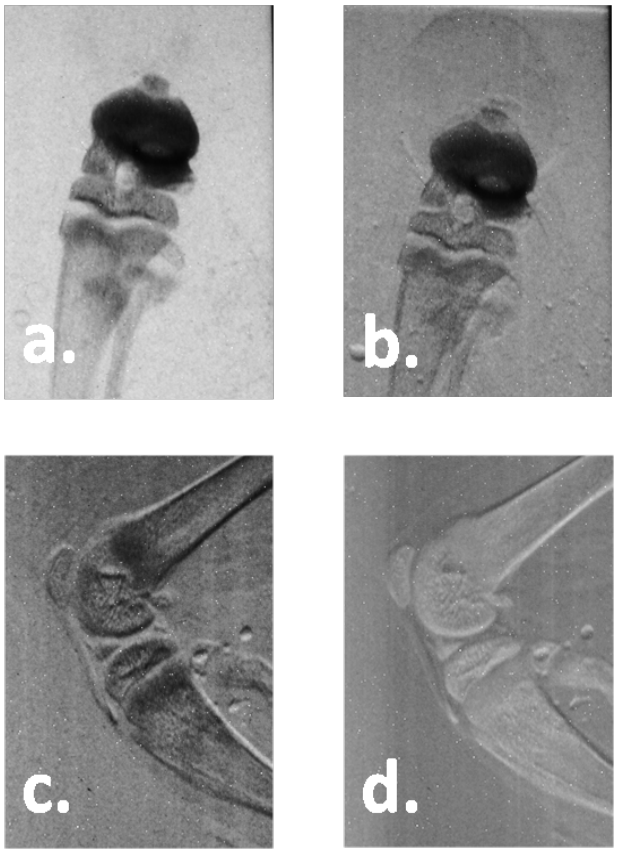

Figure 30 DEI Images of a juvenile rat, 2 weeks post fracture, 2nd batch. These images were acquired at the BMIT Bend Magnet beamline at 41keV using the Si (3,3,3) monochromator – analyzer set. Figures a and b are coronal views and figures c, d are sagittal views. Figure a is taken at the analyzer top location. Figure b and c are taken at the side of the analyzer rocking curve. Figure d is taken in the analyzer wings.

based Nesch DEI system and the laboratory based microCT. The images were acquired on the bend magnet beamline 05-BM-1. The beam was prepared and analyzed by a silicon (4,4,0) monochromator and analyzer crystal set. It should be noted that this is a departure from both the NSLS and Nesch systems which are silicon (3,3,3) based systems. In terms of predicted sensitivity there is a loss of refraction contrast of 10.3% in using the silicon (4,4,0) compared to the (3,3,3) reflection planes. This choice was made by the beamline designers. The images of the rat tibia – fibula specimen are shown in Figure 30. As seen in this figure, the images are comparable to the planar images acquired at NSLS and indicate that the crystal choice has had minimal impact on planar DEI. Planned DEI CT in other projects should determine if this crystal configuration provides quality images.

4.5 SkyScan micro-CT Data (Second Batch)

The images produced in the Micro-CT system were high quality detailed absorption contrast images. The growth plate and trabecular bone detail is high. Note the indistinct line between the bone of the

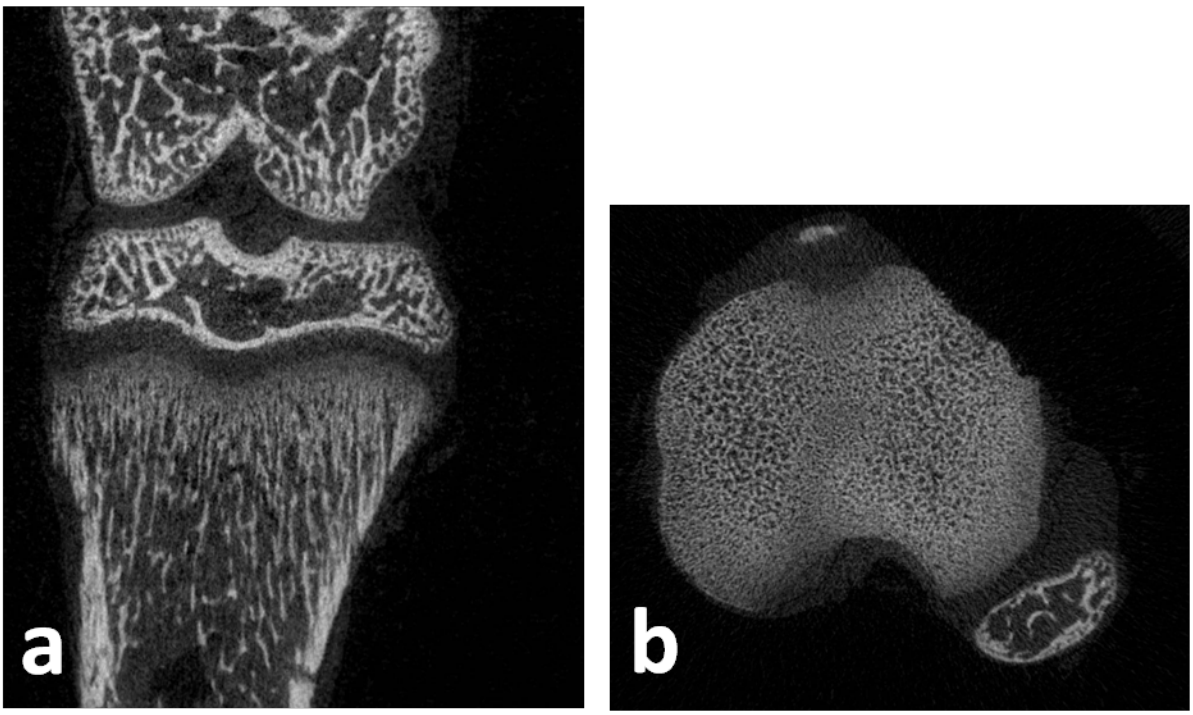

Figure 31 SkyScan micro-CT image growth plate specimen (second batch rat specimens) with 10 micron voxel size {a) coronal plane, b) axial plane}.

growth plate metaphysis adjacent to the zone of provisional calcification of the growth plate itself in the coronal image. This represents the zone where the cartilaginous growth plate starts to ossify. In the

refraction images above a sharp refraction plane was produced illustrating the unique features of refraction contrast compared to absorption contrast.

5 Discussion

In this chapter the results obtained by DEI will be discussed in some detail. The unique feature of this work compared to conventional imaging is understanding and interpretation of refraction contrast in the image.

5.1 Diffraction Enhanced Imaging Interpretation

The diffraction enhanced imaging method results in the derivation of two unique images. One is similar to absorption imaging – the apparent absorption, and one unique image – the refraction angle image.

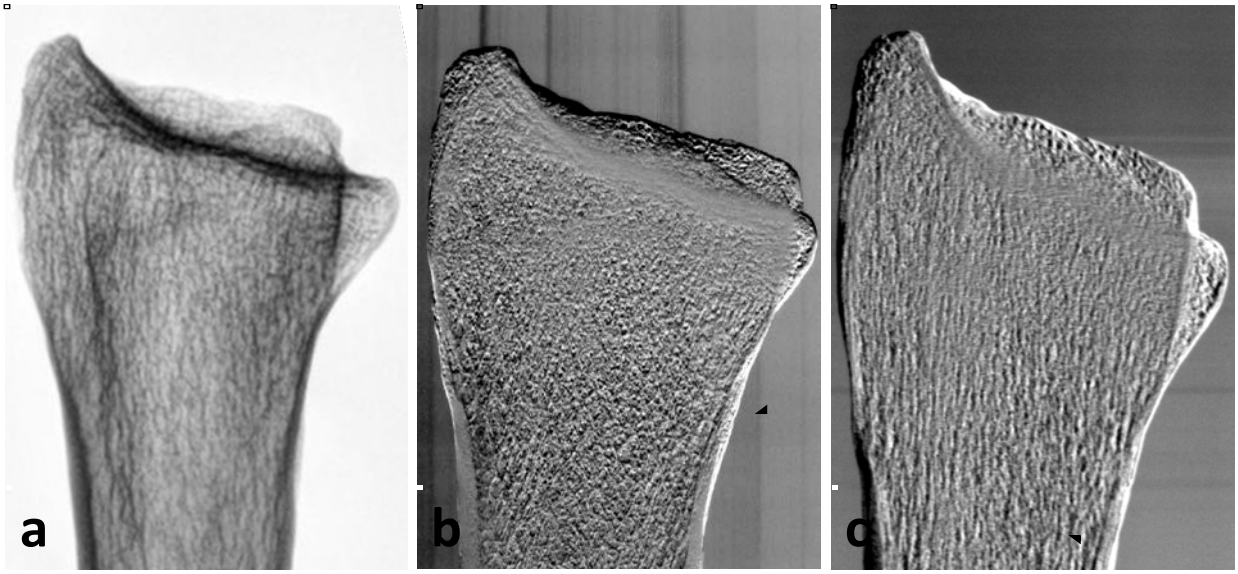

Figure 32 Images of a dry specimen of a human cadaveric radius. Figure a is a conventional radiograph. Figure b and c are DEI images of the same specimen with orthogonal orientations. In figure b the long axis of the radius is parallel to the refraction direction. Figure c is with the long axis rotated 90 degrees. The arrows show the direction of refraction sensitivity. (Cooper *et al.*, 2010)

The apparent absorption image will contain the absorption contrast as in conventional imaging but will also include additional contrast from a form of extreme scatter rejection referred to as extinction contrast (Hayat, 2007). Since the image has two sources of contrast, the term apparent absorption

contrast was coined to indicate that more than absorption is contributing to contrast. In many instances the extinction contrast mechanism contributes more to the contrast in these images. However, this effect is only noticeable when the apparent absorption image is compared to a conventional radiograph.

The directional sensitivity of refraction contrast appears when visualizing the structure of bone due to the orientation of the trabeculae. This effect is shown in the DEI images of Figure 32b and c. Figure a is a conventional radiograph. The arrows in the DEI images show the refraction sensitive direction which is vertical in b and horizontal in c. The background lines are transient artifacts of the DEI imaging system. The refraction contrast is only visualized when the tissue interface occurs parallel to the refraction direction (i.e. then there is a spatial gradient in the projected density along the refraction direction). If the tissue interface is vertical there is no refraction contrast detectable when the refraction direction is vertical.

Careful inspection of Figure 32 shows some interesting differences which should be discussed. There is a strong orientation difference in contrast between the two DEI images shown in figures b and c. Refraction contrast is extremely sensitive to the orientation of the object relative to the direction of refraction which is shown in more detail in Figure 33. This figure highlights three regions of interest in the radius. The oval highlights the growth plate scar, the rectangle the articular surface of the bone and the diamond the trabecular pattern of the metaphysis.

Within the oval the conventional radiograph has slightly increased density in a linear orientation perpendicular to the long axis of the bone which represents residual calcium deposits along the growth plate as it closed. In Figure 33b the refraction contrast of the growth plate scar is visible because the refraction occurs parallel to the sensitive direction. In Figure 33c the growth plate scar is oriented in the same orientation as the refraction sensitive direction and as a result no contrast is visible.

Within the rectangular region is the bony articular surface which creates a strong interface of more dense calcium along the perpendicular direction to the long axis of the bone. On the radiograph (a) the

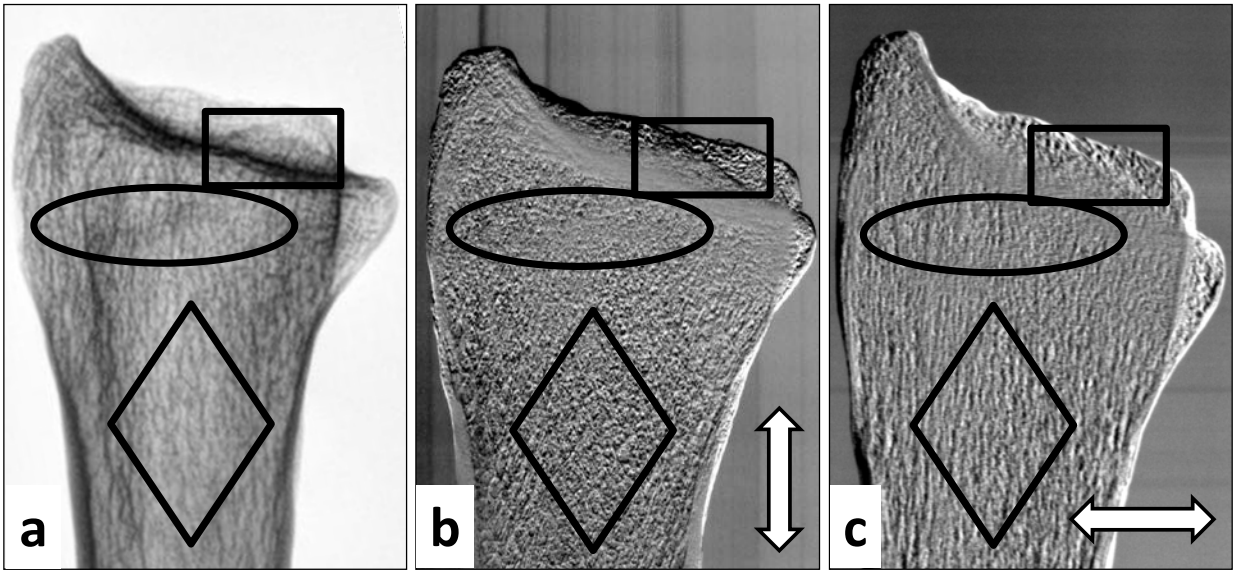

Figure 33 Overlay of regions of interest on Figure 27. The oval region highlights the growth plate scar, the square highlights the articular surface of the bone and the diamond highlights the trabecular pattern of the metaphysis {adapted from (Cooper *et al.*, 2010)}.

relative density appears as darker, whereas in the refraction images the contrast occurs at the edge of the more dense bone and relatively little contrast within the more solid component (i.e. when compared with the darkest region in the rectangular box in a).

In the metaphysis, the centrally located diamond contains a typical trabecular appearance with more linear trabeculae parallel to the long axis of the bone (along the lines of stress) with smaller crossing trabeculae between the larger more dominant trabeculae. The absorption radiograph (a) shows the trabecular pattern such that the more dense trabeculae along the long axis are more visible because of the relatively increased absorption contrast. In figure b, the refraction contrast with the sensitive direction parallel to the long axis selectively demonstrates the smaller trabeculae perpendicular to the shaft of the bone. In figure c, the refraction contrast of the larger trabeculae is prominently seen in the sensitive direction of refraction which is parallel to the long axis of the bone.

For clarity, please note that the refraction sensitive direction identifies the direction along which the system is sensitive to changes in density and thickness variations. This effect leads to visualizing features which are primarily perpendicular to that direction.

5.2 DEI-CT

In conventional absorption CT imaging, the attenuation of radiation through an object using a filtered back projection algorithm is used to produce the image(Natterer, 1986). The various areas of increased

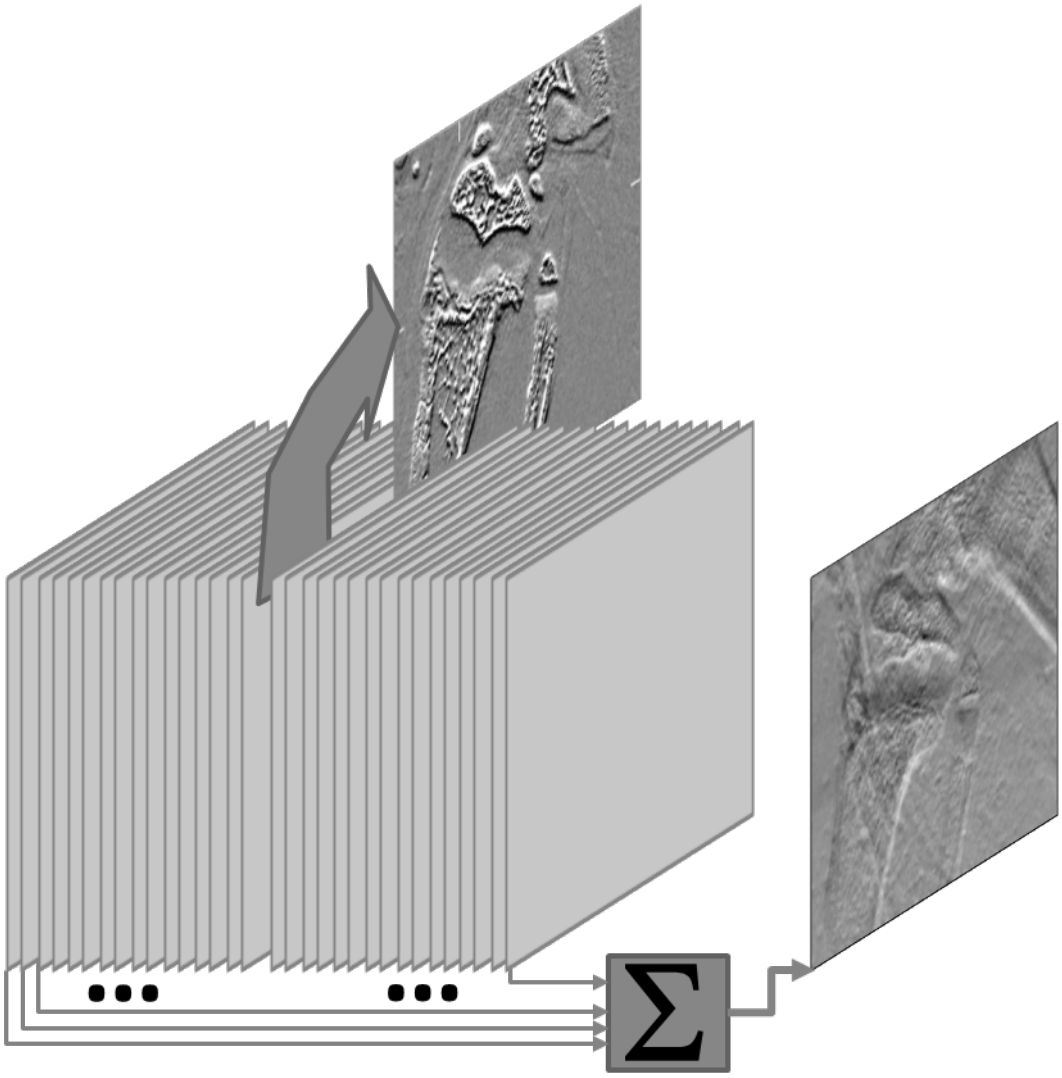

Figure 34 Relationship between reconstructed planes of a CT image and the corresponding projection image for an object. Example is for a DEI CT refraction image.

attenuation or decreased attenuation will produce areas of increased density or decreased density in the image respectively.

Nearly the same thing happens with DEI-CT however the contrast in the image is based on the refraction (change in direction) of the x-ray photon across an interface. The planar images represent the sum of all

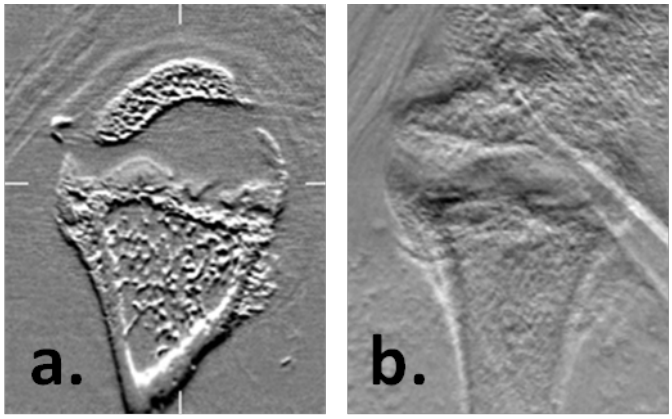

Figure 35 DEI CT sagittal plane image (a) and corresponding DEI projection (b) refraction images.

the refraction events prior to hitting the detector. This effect is shown in Figure 34. Using DEI-CT image planes can be reconstructed from the three dimensional volume of data (x, y and projection angle) and demonstrate the refraction contrast within a thin plane removing the refraction contrast outside the plane of interest from the image. The refraction sensitive plane is the primary direction of refraction contrast, but is it has shown (Dilmanian *et al.*, 2000) that the angle of the tissue interface within the

Figure 36 DEI CT coronal section (a) compared with DEI coronal projection (b) refraction images.

object can also produce refraction contrast perpendicular to the refraction sensitive plane when using DEI-CT.

This produces a clearer understanding of the anatomy and one can examine the refraction contrast of small structures that would be lost in the noise of a planar image. Here is where the real potential of

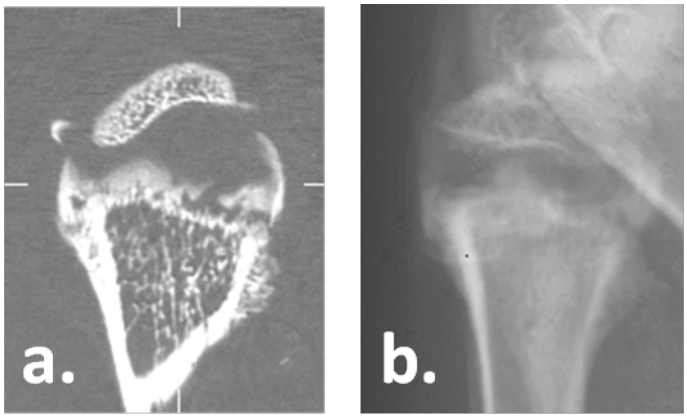

Figure 37 DEI CT sagittal section (a) compared with DEI sagittal projection (b) apparent absorption images

DEI imaging lays – the ability to visualize the tiny micro-structures that may be able to produce refraction contrast but are not large or dense enough to produce absorption contrast.

This is demonstrated in Figure 36 where the coronal section clearly shows tiny changes in refraction contrast which are otherwise completely obscured in the projection image as a result of the multiple

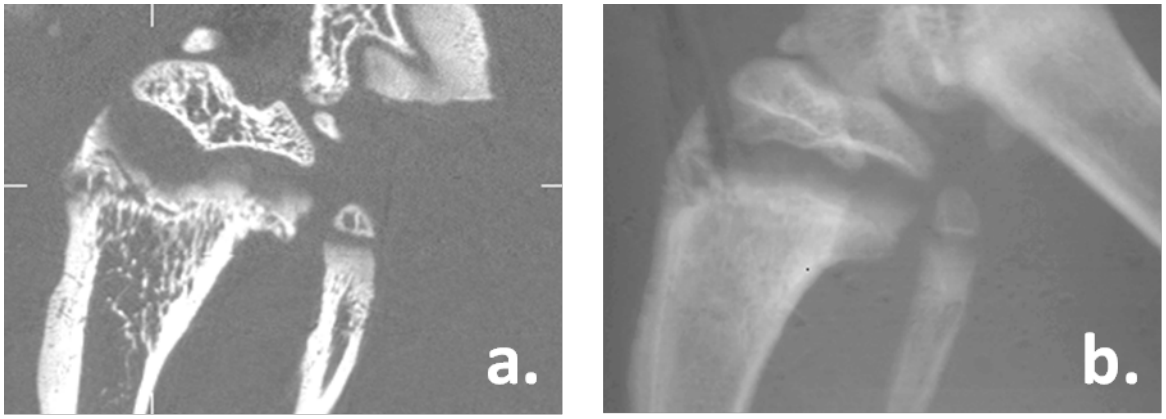

Figure 38 DEI CT coronal section (a) compared with DEI coronal projection (b) apparent absorption images.

refractions that occur through the thickness of the object on either side of the slice shown in figure a.

Similarly, in the sagittal plane more detail is visible on the DEI CT slice as shown in Figure 35 compared to the corresponding sagittal projection image.

The apparent absorption images seen in Figure 37 (sagittal) and Figure 38(coronal) are nearly the same as what would be seen in a clinical absorption CT setting (figure a). The tiny changes in absorption contrast are also more easily detected compared to the absorption projection image (figure b) which is why CT is such a powerful technique compared to projectional images.

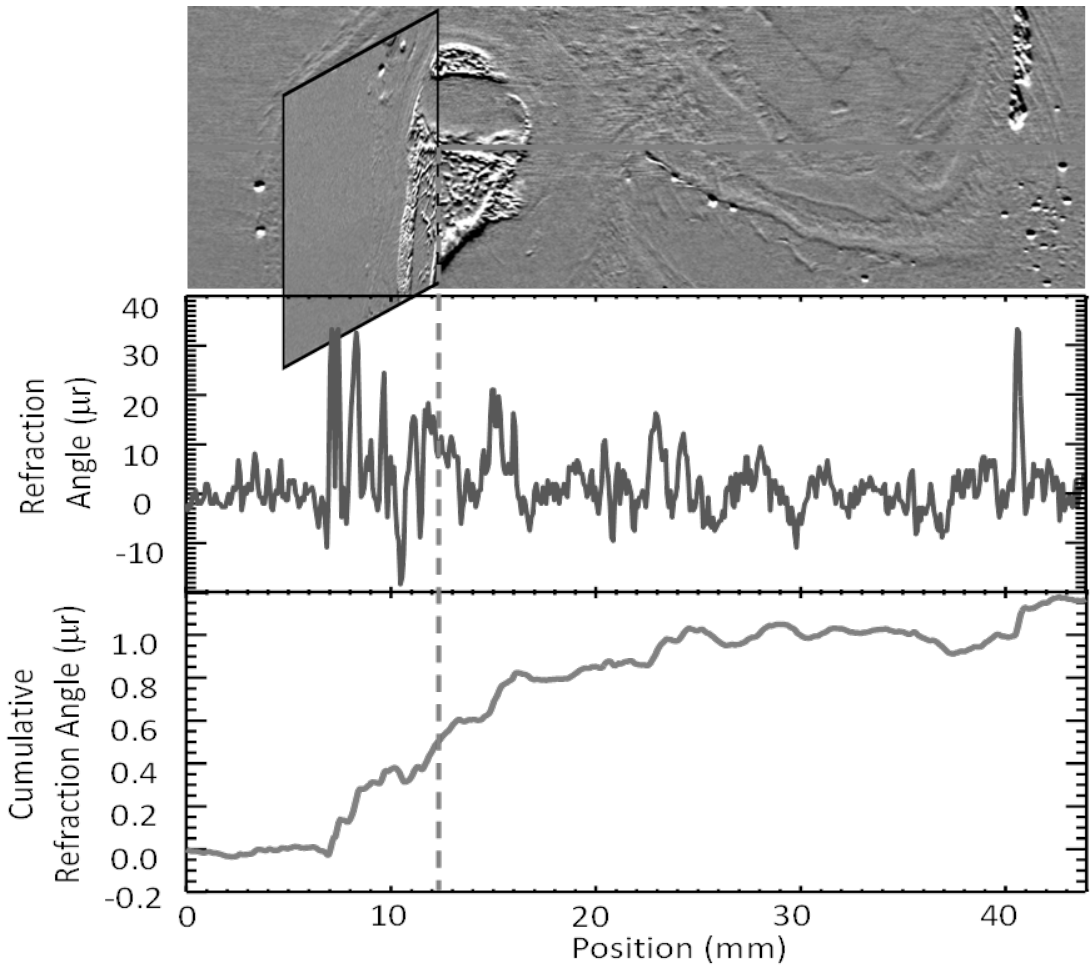

Figure 39 Composite figure with the top image showing a photon trajectory in the sagittal plane of the tibia with a coronal plane intersecting at the fracture site. Below are refraction angle plots for photon trajectory. The top plot is the refraction angle for each interaction. The bottom plot is the cumulative angle of the trajectory across the sagittal section.

6 Conclusion

This work was originally intended to apply a unique imaging technique for the study of growth plate fracture pathophysiology. However, it became clear that the technical image production and interpretation was more important to the project than the individual analysis of each specimen. It is recognized that our initial hypothesis was not addressed and that the results and course of work took a different direction. As a result the specimens selected were used to refine the technique and interpret the synchrotron based images compared to conventional images. Therefore the hypothesis evolved into an observational study to understand the relationship of the refraction image to the object. In essence, to better understand how to interpret refraction images. It was found that x-ray refraction images are less intuitive to understand than x-ray absorption images.

Using the refraction of x-rays to produce contrast definitely provides unique images with great detail. The concept of using the change in direction of the x-ray photon (refraction) as the source of image contrast to visualize tissue edges and not be limited to the attenuation of x-ray photons to provide absorption contrast remains a powerful and unique potential imaging tool. We found that in planar DEI, the orientation of the object significantly affects the image contrast since the edges within the object perpendicular to the refraction plane will not produce contrast on the final image, however those edges parallel to the refraction plane with result in strong refraction contrast. A variable degree of refraction edge contrast occurs in between the perpendicular and parallel planes depending on the relationship of the tissue interface and the refraction sensitive direction. Long bones and the growth plate itself have many parallel edges and interpreting the images that are produced requires a significant technical understanding of how the image is acquired as well as a strong preliminary understanding of the anatomy of the object being imaged. Perhaps a standardized imaging routine could be developed where, like conventional radiography, one would image an object in orthogonal planes and with the long axis of the object imaged parallel and 90 degrees relative to the angle of refraction. These standards may become specific to the object being imaged, but for long bones this seems reasonable.

The animal model that was used was a rat and the growth plates of the tibia in these animals are small. The imaging techniques are still experimental and each time a series of images are obtained there are a number of variables that can affect the quality. The variable technical factors that produce the refraction contrast will likely be easier to appreciate in the images of a larger specimen. Once the

technique has been optimized and fully understood how to interpret the images, a smaller animal model for further work on sequential imaging using potential therapeutic models could be pursued.

The development of a table top version of DEI using a conventional x-ray tube source does have some potential but will require a significantly higher energy tube producing higher flux of photons than what was used for the preliminary imaging trials in this project. The images presented from the table top system in section 4.3 took most of one day to acquire due the lack of sufficient flux from the x-ray tube. Overcoming the flux limitation will take further research and development. The unique potential of a laboratory based system is that it could potentially be mounted onto a frame which could be rotated. The system refraction plane could then be changed depending on the orientation of the object to be imaged, therefore optimizing the refraction contrast for the imaging indication. In addition refraction images could be obtained in different refraction planes on the same object therefore improving the image analyses and perhaps better understanding of the refraction characteristics of the object.

A clearer understanding of how to interpret the refraction based images, particularly using CT, will potentially be useful for research applications of synchrotron-based imaging. The CT image allows one to focus on the refraction contrast in one slice removing the "noise effect" from the rest of the tissue. On these images the interpreter can get a better appreciation of the anatomy including tiny interfaces that produce refraction contrast but would not have enough density difference from adjacent tissue to produce absorption contrast. In addition it was confirmed that refraction contrast perpendicular to the refraction sensitive direction could be appreciated in a CT image. This phenomenon is thought to be due to the effects of refraction contrast produced from all the projections around the object needed to produce the CT image. This realization is exciting since this technique may allow one to visualize tiny structures within tissue and become a unique imaging method such as in potentially tracking tagged cells in Molecular Imaging experiments that may not be detectable by other imaging methods (including absorption CT) and correlation with other more conventional Molecular Imaging techniques (such as PET-CT and MRI). There are limitations to this technique which will need to eventually be overcome. One is the time required to produce these data sets. Currently the time required to produce a DEI-CT data set will not permit live animal imaging. In addition, when live animals are used, the radiation dose to the tissue over such a long period of time would not be permitted ethically. However, with increased experience and practice using these methods we will become more efficient and effective.

In the near term, the potential clinical translation of synchrotron imaging will probably be primarily in using these techniques to study clinically relevant questions rather than direct clinical application. If a robust lab based system is built that can rotate and is stable enough to produce high quality refraction images, then there is a potential for DEI to be useful for selected clinical application.

7 Future Work

I am part of the Bone Imaging group of the University of Saskatchewan and am directly participating in a project funded by the Canadian Arthritis Network (PI Dr. Rosenberg) where we will use synchrotron imaging to study arthritis in a piglet animal model. We intend to develop standards and criteria that may help to interpret images of the bone-cartilage interface, which should be similar to articular cartilage and growth plate cartilage. Some standard images may be to orientate the object parallel and 90 degrees relative to the angle of refraction. However, the helpfulness of these standards may be quite specific to the object imaged depending on shape and orientation of the majority of refraction interfaces.

A larger animal model would likely provide better detail. Currently, I am working on a project imaging piglet joints which might be good model for growth plate imaging. However, at this time there is insufficient information to determine if this animal model might work for growth plate imaging. Also, larger animal models would need to include more expertise, such as animal care, anaesthesia, animal restraint and veterinary medicine support. More expert support for ethical animal care and the development of an interdisciplinary research team will produce more robust results. Also, once the imaging techniques and interpretation of the images becomes reasonably confident, then using this imaging modality for monitoring and evaluation of disease states and following the changes of potential therapeutic intervention will become possible.

A more detailed study of refraction contrast in DEI-CT will be undertaken. The concept of the primary angle of refraction and the ability of DEI-CT to detect subtle refraction contrast perpendicular to the primary angle of refraction, depending on the angle of the object, is a concept in its infancy. More work will be done using phantoms (standardized test objects) and structured objects to more completely describe these features which will be necessary to validate and support the interpretation of these images. Additional experiments with DEI-CT and correlation with conventional imaging to build a standard of interpretation guidelines or principles is planned in isolation as well as with other Synchrotron based imaging projects that I am or will become involved in. I will explore the potential of DEI-CT in molecular imaging research through the newly formed Canadian Molecular Imaging Network.

In anticipation of the insertion-device beamline at BMIT, much more innovative imaging science will be possible.

Over the course of this period I have become integrated with the Synchrotron Bio-Medical Imaging program and have become something of a bridge between clinical medical practice and imaging research at the CLS. I was appointed as a Special Advisor to the Vice-President of Research at the University of Saskatchewan (October 2010) and am an elected member of the BMIT Executive committee. Through these relationships and institutional positions I expect to be directly or indirectly involved in many of the biomedical imaging projects at BMIT for years. I intend to build on my technical understanding of synchrotron imaging methods, correlate and integrate with conventional clinical imaging methods and work to become a strong link in the local, national and international imaging network.

8 References

Alexander C J 1976 Effect of growth rate on the strength of the growth plate-shaft junction *Skeletal Radiology* **1** 67-76

Als-Nielsen J and McMorrow D 2001 *Elements of modern X-ray physics* (New York: Wiley) section 3.1, p63 (refraction); section 5.4.1, p184 (Darwin width)

Azároff L V 1974 *X-Ray Diffraction* (International Series in Pure and Applied Physics, McGraw-Hill) chapter 2, pp 222-294 (Darwin width); section 7.III.B.5, p 544 (multiple crystal rocking curve)

Barmada A, Gaynor T and Mubarak S J 2003 Premature physeal closure following distal tibia physeal fractures: a new radiographic predictor *J Pediatr Orthop* **23** 733-9

Batterman B W and Cole H 1964 Dynamical Diffraction of X-Rays by Perfect Crystals *Reviews of Modern Physics* **36** 681-717

Bragg W H 1913a The reflection of X-rays by crystals. *Nature* **91** 477

Bragg W H 1913b X rays and crystals *Nature* **90** 219

Bushberg J T, Siebert J A, Liedholdt Jr. E M and Boone J M eds 2001 *The Essential Physics of Medical Imaging* (Lippincott Williams & Wilkins) p164 (contrast)

Bushuev V A, Ingal V N and Beliaevskaya E A 1996 Dynamical theory of images generated by noncrystaline objects for the method of phase-dispersive introscopy *Crystallography Reports* **41** 659-63

Chapman D 2011 Biomedical Engineering 850 Class Notes. ed S Wiebe (Saskatoon, SK) - non refereed

Chapman D, Thomlinson W, Johnston R E, Washburn D, Pisano E, Gmur N, Zhong Z, Menk R, Arfelli F and Sayers D 1997 Diffraction enhanced x-ray imaging *Phys Med Biol* **42** 2015-25

Chung R, Cool J C, Scherer M A, Foster B K and Xian C J 2006 Roles of neutrophil-mediated inflammatory response in the bony repair of injured growth plate cartilage in young rats *J Leukoc Biol* **80** 1272-80

Compton A H 1924 A general quantum theory of the wave-length of scattered X-rays *Phys Rev* **24** 168-176

Cooper D M, Bewer B, Wiebe S, Wysokinski T W and Chapman D 2010 Diffraction Enhanced X-ray Imaging of the Distal Radius: A Novel Approach for Visualization of Trabecular Bone Architecture *Can Assoc Radiol J* **62** 251-5

Darwin C G 1914a The theory of x-ray reflection *Phil. Mag.* **27** 315-33

Darwin C G 1914b The theory of x-ray reflection, Part II *Phil. Mag.* **27** 675-90

Dilmanian F A, Zhong Z, Ren B, Wu X Y, Chapman L D, Orion I and Thomlinson W C 2000 Computed tomography of x-ray index of refraction using the diffraction enhanced imaging method *Phys Med Biol* **45** 933-46

Ewald P P 1916a Zur Begründung der Kristalloptik. I. Theorie der Dispersion *Ann. Physik* **49** 1-38

Ewald P P 1916b Zur Begründung der Kristalloptik. II. Theorie der Reflexion und Brechung *Ann. Physik* **49** 117-43

Ewald P P 1917 Zur Begründung der Kristalloptik. III. Röntgenstrahlen *Ann. Physik* **54** 519-97

Gotzsche P C and Olsen O 2000 Is screening for breast cancer with mammography justifiable? *Lancet* **355** 129-34

Haines R W 1976 Destruction of hyaline cartilage in the sigmoid notch of the human ulna *J Anat* **122** 331-4

Hasnah M O, Zhong Z, Oltulu O, Pisano E, Johnston R E, Sayers D, Thomlinson W and Chapman D 2002 Diffraction enhanced imaging contrast mechanisms in breast cancer specimens *Med Phys* **29** 2216-21

Haus A G and Cullinan J E 1989 Screen film processing systems for medical radiography: a historical review *Radiographics* **9** 1203-24

Hayat M A 2007 *Cancer Imaging: Instrumentation and Applications* (Elsevier, Academic Press) Chapter 2.2, pp119-26

Hefti F, von Laer L and Morscher E 1991 [Principles and pathogenesis of post-traumatic axial malalignment in the growth years] *Orthopade* **20** 324-30

Hendee W R and Ritenour E R 2002 *Medical imaging physics* (Wiley-Liss) p119 (x-ray interactions with matter); p58 (photoelectric effect); p59-63 (Compton effect); p227-8 (Anti-scatter grids); p55 (exponential attenuation)

Honorati M C, Cattini L and Facchini A 2004 IL-17, IL-1beta and TNF-alpha stimulate VEGF production by dedifferentiated chondrocytes *Osteoarthritis Cartilage* **12** 683-91

Ingal V N and Beliaevskaya E A 1995 X-ray plane-wave topography observation of phase contrast from a non-crystalline object *J. Phys. D: Appl. Phys* **28** 2314-7

Maes C, Stockmans I, Moermans K, Van Looveren R, Smets N, Carmeliet P, Bouillon R and Carmeliet G 2004 Soluble VEGF isoforms are essential for establishing epiphyseal vascularization and regulating chondrocyte development and survival *J Clin Invest* **113** 188-99

Muehleman C, Li J and Zhong Z 2006 Preliminary study on diffraction enhanced radiographic imaging for a canine model of cartilage damage *Osteoarthritis Cartilage* **14** 882-8

Natterer F 1986 *The Mathematics of Computerized Tomography* (New York, N.Y.: John Wiley & Sons) p81 (filtered back projection)

Nesch I, Fogarty D P, Tzvetkov T, Reinhart B, Walus A C, Khelashvili G, Muehleman C and Chapman D 2009 The design and application of an in-laboratory diffraction-enhanced x-ray imaging instrument *Rev Sci Instrum* **80** -

Oltulu O, Zhong Z, Hasnah M, Wernick M N and Chapman D 2003 Extraction of extinction, refraction and absorption properties in diffraction enhanced imaging *Journal of Physics D: Applied Physics* **36** 2152-6

Oppelt A 2005 *Imaging systems for medical diagnostics: fundamentals, technical solutions, and applications for systems applying ionizing radiation, nuclear magnetic resonance, and ultrasound* 2nd Edition (Wiley - VCH) p350 (radiography systems)

Pagot E, Cloetens P, Fiedler S, Bravin A, Coan P, Baruchel J, Hartwig J and Thomlinson W 2003 A method to extract quantitative information in analyzer-based x-ray phase contrast imaging *Applied Physics Letters* **82** 3421

Pisano E D, Johnston R E, Chapman D, Geradts J, Iacocca M V, Livasy C A, Washburn D B, Sayers D E, Zhong Z, Kiss M Z and Thomlinson W C 2000 Human breast cancer specimens: diffraction-enhanced imaging with histologic correlation--improved conspicuity of lesion detail compared with digital radiography *Radiology* **214** 895-901

Podurets K M, Somenkov V A and Sh. Shil'shtein S 1989 Refraction-contrast radiography *Sov. Phys. Tech. Phys.* **34** 654

Roentgen W C 1896 On a New Kind of Rays *Science* **3** 227-31

Somenkov V A, Tkalich A K and S. S S s 1991 Refraction contrast in x-ray introscopy *Sov. Phys. Tech. Phys.* **36** 1309-11

Wernick M N, Wirjadi O, Chapman D, Zhong Z, Galatsanos N P, Yang Y Y, Brankov J G, Oltulu O, Anastasio M A and Muehleman C 2003 Multiple-image radiography *Phys Med Biol* **48** 3875-95

Williams K E 2006 *Fractures in Children,* ed C A Rockwood*, et al.* (Philidelphia: Lippencott-Raven) pp 3-20

Xian C J, Zhou F H, McCarty R C and Foster B K 2004 Intramembranous ossification mechanism for bone bridge formation at the growth plate cartilage injury site *J Orthop Res* **22** 417-26

Zhong Z, Thomlinson W, Chapman D and Sayers D 2000a Implementation of diffraction-enhanced imaging experiments: at the NSLS and APS *Nuclear Instruments & Methods in Physics Research A* **450** 556

Zhong Z, Thomlinson W, Chapman D and Sayers D 2000b Implementation of diffraction-enhanced imaging experiments: at the NSLS and APS *Nucl Instrum Meth A* **450** 556-67

Zhou F H, Foster B K, Sander G and Xian C J 2004 Expression of proinflammatory cytokines and growth factors at the injured growth plate cartilage in young rats *Bone* **35** 1307-15